

# ICES REPORT 16-04

---

February 2016

## Pressure and fluid-driven fracture propagation in porous media using an adaptive finite element phase field model

by

Sanghyun Lee, Mary F. Wheeler, Thomas Wick



**The Institute for Computational Engineering and Sciences**  
The University of Texas at Austin  
Austin, Texas 78712

*Reference: Sanghyun Lee, Mary F. Wheeler, Thomas Wick, "Pressure and fluid-driven fracture propagation in porous media using an adaptive finite element phase field model," ICES REPORT 16-04, The Institute for Computational Engineering and Sciences, The University of Texas at Austin, February 2016.*

# Pressure and fluid-driven fracture propagation in porous media using an adaptive finite element phase field model

Sanghyun Lee <sup>\*</sup>      Mary F. Wheeler <sup>†</sup>      Thomas Wick <sup>‡</sup>

This work presents phase field fracture modeling in heterogeneous porous media. We develop robust and efficient numerical algorithms for pressure-driven and fluid-driven settings in which the focus relies on mesh adaptivity in order to save computational cost for large-scale 3D applications. In the fluid-driven framework, we solve for three unknowns pressure, displacements and phase-field that are treated with a fixed-stress iteration in which the pressure and the displacement-phase-field system are decoupled. The latter subsystem is solved with a combined Newton approach employing a primal-dual active set method in order to account for crack irreversibility. Numerical examples for pressurized fractures and fluid filled fracture propagation in heterogeneous porous media demonstrate our developments. In particular, mesh refinement allows us to perform systematic studies with respect to the spatial discretization parameter.

**Keywords:** Phase Field; Fluid Filled Fracture; Adaptive Finite Elements; Porous Media; Primal-Dual Active Set

## 1 Introduction

Crack propagation in brittle and porous media is currently one of the major research topics in mechanical, energy, and environmental engineering. In this paper, we concentrate specifically on fracture propagation in three dimensional heterogeneous porous media. We consider a variational approach for brittle fracture introduced by Francfort and Marigo [18] that is formulated in terms of a thermodynamically-consistent phase field technique; see Miehe et al. [32]. Other approaches for treating pressurized fracture include the following: cohesive zone finite elements (CZ-FEM) [17], displacement discontinuity methods (DDM) [40, 44, 56], partition-of-unity methods and closely related XFEM/GFEM (extended and generalized finite elements) methods [21, 22, 23, 29, 45, 46, 50]. Boundary element methods have been employed in [15, 19], and peridynamics for hydraulic fracturing has been considered in [27]. Discrete networks of fluid filled fractures have been investigated in [8, 28, 30, 39, 47].

---

<sup>\*</sup>Center for Subsurface Modeling, The Institute for Computational Engineering and Sciences, The University of Texas at Austin, Austin, Texas 78712, USA

<sup>†</sup>Center for Subsurface Modeling, The Institute for Computational Engineering and Sciences, The University of Texas at Austin, Austin, Texas 78712, USA

<sup>‡</sup>RICAM, Austrian Academy of Sciences Altenberger Str. 69 4040 Linz, Austria

---

Our motivations for employing a phase field model are that fracture nucleation, propagation, kinking, and curvilinear paths are automatically included in the model; post-processing of stress intensity factors and remeshing resolving the crack path are avoided. Furthermore, the underlying equations are based on continuum mechanics principles that can be treated with adaptive Galerkin finite elements. In fact, variational and phase field formulations for fracture are active research areas as attested in recent years; see Bourdin et al. [10, 11], Miehe et al. [31, 32, 33], Borden et al. [9], Artina et al. [6], Burke et al. [14], Allaire et al. [1], Schlüter et al. [48], Ambati et al. [2], Mikelić et al. [36, 38]. Here, discontinuities in the displacement field across the lower-dimensional crack surface are approximated by an auxiliary phase field function. The latter can be viewed as an indicator function, which introduces a diffusive transition zone between the broken and the unbroken material.

For pressurized fractures in porous media, the pressure is a fixed, given quantity or assumed to be computed [38, 52]. The essential aspects of a phase field-based pressurized-fracture propagation formulation are techniques that must include resolution of the length-scale parameter  $\varepsilon$ , the numerical solution of the forward problem and enforcement of the irreversibility of crack growth. The sum of these requirements leads to a variational inequality. For numerical simulations, a robust computational framework in terms of a quasi-monolithic formulation has been proposed in [24] in which a primal-dual active set method (i.e., a semi-smooth Newton method [26]) is coupled with the Newton solver for the nonlinear forward problem.

Our main attention in this paper is on three-dimensional applications that are challenging because of computational cost. This is especially the case for phase-field problems because the resolution of the crack requires (very) fine meshes. Here, uniform refinement is infeasible and we adopt a method proposed in [24] for two-dimensional problems and extend these ideas to three-dimensional applications. The efficiency is shown in terms of pressurized and fluid-filled phase-field fractures for which systematic 3D studies including mesh refinements are not present in the literature.

In summary, the goal and novelty of the present paper are systematic studies of computational stability using predictor-corrector mesh adaptivity for three-dimensional pressure and fluid-driven phase-field fracture problems. Such studies are essential for better understanding between model and discretization parameters in phase-field modeling for the previously mentioned applications. We emphasize that the fluid-filled fracture framework in porous media (with Biot's coefficient  $\alpha = 1$ ) is itself novel where we formulate a fixed-stress iteration for the pressure system coupled to the fully-coupled displacement-phase-field system. Here, the latter system is treated with a primal-dual active set method. This idea is in contrast to the fluid-filled phase-field fracture framework presented in [37] in which all equations have been decoupled.

The outline of this paper is as follows: We first state the governing equations in Section 2. Then, we present our main algorithm and adaptive discretization in Section 3. In Section 4, we provide numerical examples that demonstrate the potential of this approach for treating practical engineering applications.

## 2 Mathematical Models for Pressurized and Fluid Filled Fractures

Let  $\Lambda \in \mathbb{R}^d$ ,  $d = 2, 3$  be a smooth open and bounded computational domain with Lipschitz boundary  $\partial\Lambda$  and let  $[0, T]$  be the computational time interval,  $T > 0$ . We assume that the crack  $\mathcal{C}$  is contained compactly in  $\Lambda$ . Here, we emphasize that the crack is seen as a thin three-dimensional volume where the thickness is much larger than the pore size of the porous medium. The displacement of the solid and diffusive flow in the porous medium are modeled in  $\Omega = \Lambda \setminus \bar{\mathcal{C}}$  by the classical quasi-static elliptic-parabolic Biot system for a linear elastic, homogeneous, isotropic, porous solid saturated with a slightly compressible viscous fluid for every  $t \in (0, T]$ .

---

First, we start from the constitutive equation for the Cauchy stress tensor  $\sigma^{por}$ ,

$$\sigma^{por}(\mathbf{u}, p) - \sigma_0 = \sigma(\mathbf{u}) - \alpha(p - p_0)I, \quad \text{in } \Omega \times (0, T] \quad (1)$$

where  $\mathbf{u} : \Omega \times [0, T] \rightarrow \mathbb{R}^d$  is the solid's displacement,  $p : \Omega \times [0, T] \rightarrow \mathbb{R}$  is the fluid pressure,  $\alpha \in [0, 1]$  is the Biot coefficient,  $I$  is the identity tensor,  $\sigma_0$  and  $p_0$  are the given initial values when  $t = 0$ , which are set to be zero for simplicity in this paper. The effective linear elastic stress tensor  $\sigma := \sigma(\mathbf{u})$  is

$$\sigma(\mathbf{u}) = \lambda(\nabla \cdot \mathbf{u})I + 2Ge(\mathbf{u}), \quad (2)$$

where  $\lambda, G > 0$  are the Lamé coefficients. The linear elastic strain tensor is given as

$$e(\mathbf{u}) = \frac{\nabla \mathbf{u} + \nabla \mathbf{u}^T}{2}. \quad (3)$$

Then the balance of linear momentum in the solid reads

$$-\nabla \cdot \sigma^{por}(\mathbf{u}, p) = \rho_s \mathbf{g} \quad \text{in } \Omega \times (0, T], \quad (4)$$

where  $\rho_s$  is the density of the solid and  $\mathbf{g}$  is the gravity. Next, the flow pressure equation is given by

$$\partial_t(\rho_F \varphi^*) + \nabla \cdot (\rho_F \mathbf{v}) = q \quad \text{in } \Omega \times (0, T] \quad (5)$$

where

$$\varphi^* = \varphi_0^* + \alpha \nabla \cdot \mathbf{u} + \frac{1}{M}(p - p_0) \quad (6)$$

is fluid volume fraction with  $\varphi_0^*$  initial value,  $\rho_f$  fluid density,  $q$  is the source/sink term, and Biot modulus  $M > 0$ . The velocity is defined by Darcy law,

$$\mathbf{v} = -\frac{K}{\eta}(\nabla p - \rho_F \mathbf{g}) \quad \text{in } \Omega \times (0, T], \quad (7)$$

where  $\eta$  is the fluid viscosity,  $\rho_F$  is the fluid density, and  $K$  is the permeability.

## 2.1 The Phase Field Energy Functional for Pressurized Fractures

Based on the linear momentum in the solid (4), we introduce the Francfort-Marigo functional [18], which describes the energy of a crack in an elastic medium as

$$E(\mathbf{u}, \mathcal{C}) = \frac{1}{2} \int_{\Omega} \sigma(\mathbf{u}) : e(\mathbf{u}) + G_c H^{d-1}(\mathcal{C}) \, d\mathbf{x}. \quad (8)$$

The Hausdorff measure  $H^{d-1}(\mathcal{C})$  denotes the length of the crack and is multiplied by a material property  $G_c > 0$ , that is considered in fracture mechanics to be the critical energy release rate. We consider the pressure energy by adding an additional pressure term in (1) as derived in [38, 36]. Thus we can rewrite (8) by

$$E(\mathbf{u}, p, \mathcal{C}) = \frac{1}{2} \int_{\Omega} \sigma(\mathbf{u}) : e(\mathbf{u}) \, d\mathbf{x} - \int_{\Omega} \alpha p \nabla \cdot \mathbf{u} \, d\mathbf{x} + G_c H^{d-1}(\mathcal{C}). \quad (9)$$

We introduce the continuous phase field variable  $\varphi : \Lambda \times [0, T] \rightarrow [0, 1]$  where  $\varphi(\mathbf{x}, t) = 0$  in the crack region and  $\varphi(\mathbf{x}, t) = 1$  in the unbroken material. This introduces a diffusive transition zone, which is controlled by the regularization parameter  $\varepsilon > 0$ ; see Figure 1 for details.

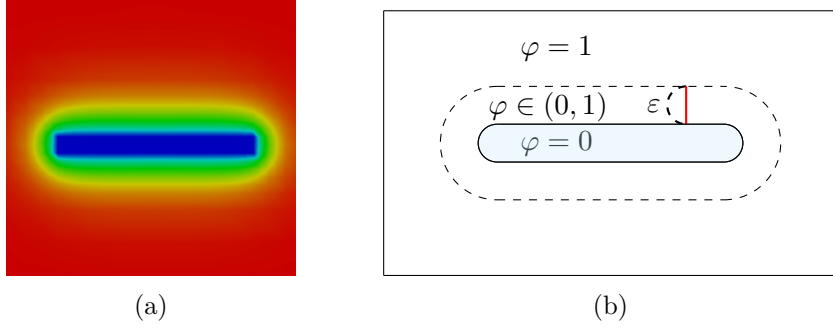


Figure 1: Fracture representation using the phase field  $\varphi$ . (a) The inner blue region indicates the crack with  $\varphi = 0$  and the outer red region indicates the unbroken zone where  $\varphi = 1$ . We have the linear diffusive transition zone near the interface of the fracture (green region). (b) Illustrates the transition zone with the thickness  $\varepsilon$ .

Before, we can write the full energy functional, we must model the interaction of fracture ( $p_F$ ) and reservoir ( $p_R$ ) pressures. This is modeled as an interface law. We assume that the fracture length (or surface area) is much larger than its width (or aperture). Therefore a lubrication approximation of the stress at the interface  $\mathcal{C}$  is a plausible choice. The fracture pressure  $p_F$  is in equilibrium with the normal component of reservoir stress at the crack  $\mathcal{C}$  such that,

$$\sigma^{por} \mathbf{n} = (\sigma(\mathbf{u}) - \alpha p_R I) \mathbf{n} = -p_F \mathbf{n}, \quad (10)$$

where  $\mathbf{n}$  is the normal unit vector. Further assuming pressure continuity at  $\mathcal{C}$  the pressure field  $p$  is such that  $p = p_F$  on  $\mathcal{C}$  and  $p = p_R$  in  $\Lambda \setminus \mathcal{C}$ . The fracture pressure contribution is reflected in the surface force integral, second term in the right hand side of the functional (9) over  $\mathcal{C}$  as:

$$\begin{aligned} \int_{\mathcal{C}} \tau \mathbf{u} \, dS &= \int_{\mathcal{C}} \sigma^{por} \mathbf{n} \mathbf{u} \, dS = - \int_{\mathcal{C}} p \mathbf{u} \mathbf{n} \, dS = - \int_{\Omega} \nabla \cdot (p \mathbf{u}) \, d\mathbf{x} + \int_{\partial\Lambda} p \mathbf{u} \mathbf{n} \, dS \\ &= - \int_{\Omega} (\mathbf{u} \cdot \nabla p + p \nabla \cdot \mathbf{u}) \, d\mathbf{x} + \int_{\partial\Lambda} p \mathbf{u} \mathbf{n} \, dS, \quad (11) \end{aligned}$$

resulting in a volumetric representation for the pressure. We assume Dirichlet boundary conditions for pressure on  $\partial\Lambda$ , and therefore the last term in (11) vanishes. Thus we have

$$\int_{\mathcal{C}} \tau \mathbf{u} \, dS = - \int_{\Lambda} (\mathbf{u} \cdot \nabla p + p \nabla \cdot \mathbf{u}) \, d\mathbf{x}.$$

We consider the global constitutive dissipation functional of Ambrosio-Tortorelli type [3, 4], for a rate independent fracture process. This means, we extend all integrals from  $\mathcal{C}$  and  $\Omega$  to  $\Lambda$ . For the elastic energy terms this has been often explained in the literature. For the pressure terms we follow [38]:

$$- \int_{\Omega} (\mathbf{u} \cdot \nabla p + p \nabla \cdot \mathbf{u}) \, d\mathbf{x} \quad \rightarrow \quad - \int_{\Lambda} \varphi^2 (\mathbf{u} \cdot \nabla p + p \nabla \cdot \mathbf{u}) \, d\mathbf{x}.$$

Then, we obtain

$$\begin{aligned} E_{\varepsilon}(\mathbf{u}, p, \varphi) &= \int_{\Lambda} \frac{1}{2} ((1-k)\varphi^2 + k) \sigma^+(\mathbf{u}) : e(\mathbf{u}) \, d\mathbf{x} + \int_{\Lambda} \frac{1}{2} \sigma^-(\mathbf{u}) : e(\mathbf{u}) \, d\mathbf{x} - \int_{\Lambda} (\alpha - 1) \varphi^2 p \nabla \cdot \mathbf{u} \, d\mathbf{x} \\ &\quad + \int_{\Lambda} (\varphi^2 \nabla p) \mathbf{u} \, d\mathbf{x} + G_c \int_{\Lambda} \left( \frac{1}{2\varepsilon} (1 - \varphi)^2 + \frac{\varepsilon}{2} (\nabla \varphi)^2 \right) \, d\mathbf{x}. \quad (12) \end{aligned}$$

---

Here  $\varepsilon$  is the thickness of the diffusive zone shown in Figure 1b and  $k$  is a small regularization parameter,  $k \ll \varepsilon$ . Regarding the stress tensor split, we follow Amor et al. [5] (see also Borden et al. [9], p. 79, for a brief discussion on the differences between different models). The stress tensor is additively decomposed into a tensile part  $\sigma^+(\mathbf{u})$  and a compressive part  $\sigma^-(\mathbf{u})$  by:

$$\sigma^+(\mathbf{u}) := \left(\frac{2}{d}G + \lambda\right)tr^+(e(\mathbf{u}))I + 2G\left(e(\mathbf{u}) - \frac{1}{d}tr(e(\mathbf{u}))I\right), \quad (13)$$

$$\sigma^-(\mathbf{u}) := \left(\frac{2}{d}G + \lambda\right)tr^-(e(\mathbf{u}))I, \quad (14)$$

where

$$tr^+(e(\mathbf{u})) = \max(tr(e(\mathbf{u})), 0), \quad \text{and} \quad tr^-(e(\mathbf{u})) = tr(e(\mathbf{u})) - tr^+(e(\mathbf{u})). \quad (15)$$

We emphasize that the energy degradation only acts on the tensile part. Finally, we assume that crack growth is irreversible. Here we follow [31, 32] and formulate the irreversibility condition as

$$\partial_t \varphi \leq 0. \quad (16)$$

The resulting system is a variational inequality that has been mathematically analyzed by Mikelić et al. [38].

## 2.2 Pressure Diffraction Equation for Modeling Fluid Filled Fractures

In order to formulate the flow equations in the porous media zone and the fracture, respectively, we employ the phase field function as an indicator function. Thus, the flow pressure equations (5)-(6) can be separated for the fracture and the reservoir sub-domain respectively.

We denote by  $\Omega_F(t)$  and  $\Omega_R(t)$  the open subsets of the space-time domain  $\Lambda \times [0, T]$  at time  $t$ .  $\Omega_R(t)$  is filled with the unbroken material (reservoir domain). In the approximation, the fracture is approximated by a volume term and  $\mathcal{C}$  becomes  $\Omega_F(t)$ . Thus, we define  $\partial\mathcal{C} := \Gamma(t) := \bar{\Omega}_F(t) \cap \bar{\Omega}_R(t)$ .

To derive the flow pressure equations for each sub-domain, first we consider the two separate mass continuity equations for the fluid in the reservoir and the fracture from (5), which we can rewrite as

$$\partial_t(\rho_F \varphi_F^*) + \nabla \cdot (\rho_F \mathbf{v}_F) = q_F - q_L \quad \text{in} \quad \Omega_F \times (0, T], \quad (17)$$

$$\partial_t(\rho_R \varphi_R^*) + \nabla \cdot (\rho_R \mathbf{v}_R) = q_R \quad \text{in} \quad \Omega_R \times (0, T]. \quad (18)$$

Here  $\varphi_R^*$  and  $\varphi_F^*$  are the reservoir and fracture fluid fraction respectively and we assume  $\varphi_F^* = 1$  (since the porosity of the fracture is one). Recall the reservoir fluid fraction is given in (6). In addition, the leak-off term  $q_L$  is defined in (31), and  $q_F$  and  $q_R$  are source/sink terms for fracture and reservoir, respectively.

Next, we describe the flow given by Darcy's law at (7) for the fracture ( $j = F$ ) and for the reservoir ( $j = R$ ), respectively by

$$\mathbf{v}_j = -\frac{K_j}{\eta_j}(\nabla p_j - \rho_j \mathbf{g}). \quad (19)$$

We assume the fluid in the reservoir and the fracture is slightly compressible, thus we define the fluid density as

$$\rho_j := \rho_j^0 \exp(c_j(p_j - p_j^0)) \approx \rho_j^0[1 + c_j(p_j - p_j^0)], \quad (20)$$

where  $\rho_j^0$  is the reference density and  $c_j$  is the fluid compressibility.

Following the general reservoir approximation with the assumption that  $c_R$  and  $c_F$  are small enough, we use  $\rho_R = \rho_R^0$  and  $\rho_F = \rho_F^0$  to rewrite the equations (17)-(18) by

$$\rho_R^0 \partial_t \left( \frac{1}{M} p_R + \alpha \nabla \cdot \mathbf{u} \right) - \nabla \cdot \frac{K_R \rho_R^0}{\eta_R} (\nabla p_R - \rho_R^0 \mathbf{g}) = q_R \quad \text{in } \Omega_R \times (0, T], \quad (21)$$

$$\rho_F^0 c_F \partial_t p_F - \nabla \cdot \frac{K_F \rho_F^0}{\eta_F} (\nabla p_F - \rho_F^0 \mathbf{g}) = q_F - q_L \quad \text{in } \Omega_F \times (0, T]. \quad (22)$$

For the fracture flow, we adopt a three-dimensional lubrication equation [37]. Inside this function, the fracture permeability is assumed to be isotropic such that

$$K_F = \frac{1}{12} w(\mathbf{u})^2,$$

where  $w(\mathbf{u}) = [\mathbf{u} \cdot \mathbf{n}]$  denotes the aperture (width) of the fracture, which means that the jump  $[\cdot]$  of normal displacements has to be computed. For calculating the aperture we apply an integral form using the phase field variable; details can be found in [51], p.51. Furthermore, we use an interpolated permeability  $K$  in the phase field transition zone, eg.  $K = \varphi K_R + (1 - \varphi) K_F$ . For  $\varphi = 1$  (in the reservoir), we have  $K_R$  and in the fracture  $\varphi = 0$ , we have  $K_F$ ; see Section 3.1 for more details.

### 2.3 Initial and Boundary Conditions

The system is supplemented with initial and boundary conditions. The initial condition for the pressure diffusion equations (21)-(22) is given by  $p_F(\mathbf{x}, 0) = p_F^0$  for all  $\mathbf{x} \in \Omega_F(t = 0)$  and  $p_R(\mathbf{x}, 0) = p_R^0$  for all  $\mathbf{x} \in \Omega_R(t = 0)$ , where  $p_F^0$  and  $p_R^0$  are smooth given pressures. Also we have  $\varphi(\mathbf{x}, 0) = \varphi^0$  for all  $\mathbf{x} \in \Lambda(t = 0)$ , where  $\varphi^0$  is a given smooth initial fracture.

For  $\mathbf{u}$  we prescribe Dirichlet boundary conditions on  $\partial\Lambda$ . Specifically, given  $\mathbf{f}_u : \partial\Lambda \rightarrow \mathbb{R}^d$  and  $f_p : \partial\Lambda_D \rightarrow \mathbb{R}$ , we require that

$$\mathbf{u} = \mathbf{f}_u \quad \text{on } \partial\Lambda \times (0, T], \quad (23)$$

$$p = f_p \quad \text{on } \partial\Lambda_D \times (0, T], \quad (24)$$

$$K_R (\nabla p_R - \rho_R^0 \mathbf{g}) \cdot \mathbf{n} = 0 \quad \text{on } \partial\Lambda_N \times (0, T], \quad (25)$$

$$[p] = 0 \quad \text{on } \Gamma \times (0, T], \quad (26)$$

$$\frac{K_R}{\mu_R} (\nabla p_R - \rho_R^0 \mathbf{g}) \cdot \mathbf{n} = \frac{K_F}{\mu_F} (\nabla p_F - \rho_F^0 \mathbf{g}) \cdot \mathbf{n} \quad \text{on } \Gamma \times (0, T], \quad (27)$$

where  $\mathbf{n}$  is the outward pointing unit normal on  $\Gamma$  or  $\partial\Lambda_N$ . The pressure boundary  $\partial\Lambda$  is decomposed into two non-overlapping components  $\partial\Lambda = \partial\Lambda_D \cup \partial\Lambda_N$  with  $\partial\Lambda_N \cap \partial\Lambda_D = \emptyset$ . For the phase field function, we prescribe homogeneous Neumann conditions on  $\partial\Lambda$  as it is usually done.

## 3 Numerical Methods, Algorithms and Discretization

We consider a mesh family  $\{\mathcal{T}_h\}_{h>0}$ , which is assumed to be shape regular in the sense of Ciarlet, and we assume that each mesh  $\mathcal{T}_h$  is a subdivision of  $\bar{\Lambda}$  made of disjoint elements  $\mathcal{K}$ , i.e., squares when  $d = 2$  or cubes when  $d = 3$ . Each subdivision is assumed to exactly approximate the computational domain, thus  $\bar{\Lambda} = \cup_{\mathcal{K} \in \mathcal{T}_h} \mathcal{K}$ . The diameter of an element  $\mathcal{K} \in \mathcal{T}_h$  is denoted by  $h$  and we denote  $h_{\min}$  for the minimum. For any integer  $k \geq 1$  and any  $\mathcal{K} \in \mathcal{T}_h$ , we denote by  $\mathbb{Q}^k(\mathcal{K})$  the space of scalar-valued multivariate polynomials over  $\mathcal{K}$  of partial degree of at most  $k$ . The vector-valued counterpart of  $\mathbb{Q}^k(\mathcal{K})$  is denoted  $\mathbf{Q}^k(\mathcal{K})$ . We define a partition of the time interval  $0 =: t^0 < t^1 < \dots < t^N =: T$  and denote the time step size by  $\delta t := t^n - t^{n-1}$ .

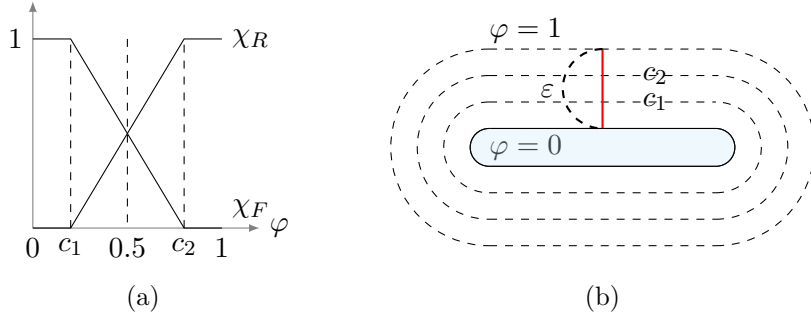


Figure 2: (a) The linear indicator functions  $\chi_F$  and  $\chi_R$  illustrated with adjustable constants  $c_1$  and  $c_2$ . (b) We consider as the fracture zone if  $\varphi \leq c_1$  and as the reservoir zone if  $\varphi \geq c_2$

### 3.1 Decomposing the Domain into $\Omega_F$ and $\Omega_R$ , Leakage Term, and Well Model

In this section, we define the fracture domain  $\Omega_F$  and the reservoir domain  $\Omega_R$  by introducing two linear indicator functions  $\chi_F$  and  $\chi_R$  for the two different sub-domains; they satisfy

$$\chi_R(\cdot, \varphi) := \chi_R(\mathbf{x}, t, \varphi) = 1 \quad \text{in} \quad \Omega_R(t), \quad \text{and} \quad \chi_R(\cdot, \varphi) = 0 \quad \text{in} \quad \Omega_F(t), \quad (28)$$

$$\chi_F(\cdot, \varphi) := \chi_F(\mathbf{x}, t, \varphi) = 1 \quad \text{in} \quad \Omega_F(t), \quad \text{and} \quad \chi_F(\cdot, \varphi) = 0 \quad \text{in} \quad \Omega_R(t). \quad (29)$$

Thus  $\chi_F(\cdot, \varphi)$  is zero in the reservoir domain and  $\chi_R(\cdot, \varphi)$  is zero in the fracture domain. In the diffusive zone, the linear functions are defined as

$$\chi_F(\cdot, \varphi) = -\frac{(\varphi - c_2)}{(c_2 - c_1)} \quad \text{and} \quad \chi_R(\cdot, \varphi) = \frac{(\varphi - c_1)}{(c_2 - c_1)}. \quad (30)$$

Thus  $\chi_R(\cdot, \varphi) = 0$  and  $\chi_F(\cdot, \varphi) = 1$  if  $\varphi(\mathbf{x}, t) \leq c_1$ , and  $\chi_R(\cdot, \varphi) = 1$  and  $\chi_F(\cdot, \varphi) = 0$  if  $\varphi(\mathbf{x}, t) \geq c_2$ , where  $c_1 := 0.5 - c_x$  and  $c_2 = 0.5 + c_x$ . For simplicity we set  $c_x = 0.1$ , and refer the reader to Figure 2 for more details.

We define the leak-off term as

$$q_L := \nabla \cdot (\rho_F \mathbf{v}_{leak}) \quad (31)$$

and the effective velocity for the fracture by

$$\mathbf{v}_F = -\frac{K_F}{\eta_F} (\nabla p_F - \rho_F \mathbf{g}) + \mathbf{v}_{leak}. \quad (32)$$

In particular, the gravity term  $\mathbf{g}^*$  is re-scaled and implicitly contains the leakage term. i.e.,  $\mathbf{g}^* := \chi_R(\cdot, \varphi) \mathbf{g} + \chi_F(\cdot, \varphi) (\mathbf{g} + (K_{eff}^{-1} / \rho_F^0) \mathbf{v}_{leak})$ , where  $K_{eff} := \chi_F(\cdot, \varphi) K_F + \chi_R(\cdot, \varphi) K_R$  including interpolation of  $K_F$  and  $K_R$  in the phase field transition zone [37].

The well terms  $q_R$  and  $q_F$  in (21)-(22) are described by suitable well models. Following Peaceman's model [16, 42, 43], we define the source term as,

$$q_F := C_j^Q (p_b - p) \times H(\mathbf{x}), \quad q_R := -C_j^Q (p_b - p) \times H(\mathbf{x}), \quad C_j^Q := \frac{2\pi \rho_i \sqrt{k_{11} k_{22}} h_3}{\mu_i \ln(r_e/r_w)}, \quad j = F, R, \quad (33)$$

where  $r_e$  is the outer equivalent radius,  $r_w$  is the inner radius, and  $h_3$  is the thickness of the well bore.  $p_b$  is a given well bore pressure and we have given anisotropic permeability  $K = \text{diag}(k_{11}, k_{22}, k_{33})$ . Here  $H(\mathbf{x})$  is defined as

$$H(\mathbf{x}) := \begin{cases} 1 & \text{if } |\mathbf{x} - \mathbf{X}| \leq c. \\ 0 & \text{otherwise,} \end{cases} \quad (34)$$

where  $c$  is a sufficiently small positive constant, and  $\mathbf{X}$  is a given source/sink point in the domain.

---

## 3.2 Discretization of the Pressure Diffraction Equation

First, we discuss temporal discretization of the pressure diffraction equations (21)-(22) and afterwards their spatial treatment.

### 3.2.1 Approximation in Space

The space approximation  $P$  of the pressure function  $p(\mathbf{x}, t)$  is approximated by using continuous piecewise polynomials given in the finite element space,

$$\mathbb{W}(\mathcal{T}) := \{W \in C^0(\bar{\Lambda}; \mathbb{R}) \mid W|_{\mathcal{K}} \in \mathbb{Q}^1(\mathcal{K}), \forall \mathcal{K} \in \mathcal{T}\}. \quad (35)$$

Assuming that the displacement field and the phase field is known, the Galerkin approximation of (21)-(22) is formulated as follows. Given  $P(\mathbf{x}, 0) = P^0$  where  $P^0$  is an approximation of the initial condition  $p^0$ , find  $P \in C^1([0, T]; \mathbb{W}(\mathcal{T}))$  such that

$$\chi_R(\cdot, \varphi) \left( \int_{\Lambda} \rho_R^0 \partial_t \left( \frac{1}{M} P + \alpha \nabla \cdot \mathbf{u} \right) \omega \, d\mathbf{x} + \int_{\Lambda} \frac{K_R \rho_R^0}{\eta_R} (\nabla P - \rho_R^0 \mathbf{g}) \nabla \omega \, d\mathbf{x} = \int_{\Lambda} q_R \omega \, d\mathbf{x} \right), \quad \forall \omega \in \mathbb{W}(\mathcal{T}), \quad (36)$$

$$\chi_F(\cdot, \varphi) \left( \int_{\Lambda} \rho_F^0 c_F \partial_t P \omega \, d\mathbf{x} + \int_{\Lambda} \frac{K_F \rho_F^0}{\eta_F} (\nabla P - \rho_F^0 \mathbf{g}) \nabla \omega \, d\mathbf{x} = \int_{\Lambda} (q_F - q_L) \omega \, d\mathbf{x} \right), \quad \forall \omega \in \mathbb{W}(\mathcal{T}). \quad (37)$$

### 3.2.2 Approximation in Time

We denote the approximation of  $P(\mathbf{x}, t^n)$ ,  $0 \leq n \leq N$  by  $P^n$ , and assume  $\mathbf{u}(t^{n+1})$  and  $\varphi(t^{n+1})$  are given values at time  $t^{n+1}$ . Then, the time stepping proceeds as follows: Given  $P^n$ , compute  $P^{n+1} \in \mathbb{W}(\mathcal{T})$  so that

$$\begin{aligned} B_R(P^{n+1})(\omega) := & \chi_R(\cdot, \varphi(t^{n+1})) \left( \int_{\Lambda} \rho_R^0 \left( \frac{1}{M} \left( \frac{P^{n+1} - P^n}{\delta t} \right) + \alpha \left( \frac{\nabla \cdot \mathbf{u}^{n+1} - \nabla \cdot \mathbf{u}^n}{\delta t} \right) \right) \omega \, d\mathbf{x} \right. \\ & \left. + \int_{\Lambda} \frac{K_R \rho_R^0}{\eta_R} (\nabla P^{n+1} - \rho_R^0 \mathbf{g}) \nabla \omega \, d\mathbf{x} - \int_{\Lambda} q_R \omega \, d\mathbf{x} \right) \quad \forall \omega \in \mathbb{W}(\mathcal{T}) \quad (38) \end{aligned}$$

$$\begin{aligned} B_F(P^{n+1})(\omega) := & \chi_F(\cdot, \varphi(t^{n+1})) \left( \int_{\Lambda} \rho_F^0 c_F \left( \frac{P^{n+1} - P^n}{\delta t} \right) \omega \, d\mathbf{x} + \int_{\Lambda} \frac{K_F \rho_F^0}{\eta_F} (\nabla P^{n+1} - \rho_F^0 \mathbf{g}) \nabla \omega \, d\mathbf{x} \right. \\ & \left. - \int_{\Lambda} (q_F - q_L) \omega \, d\mathbf{x} \right), \quad \forall \omega \in \mathbb{W}(\mathcal{T}) \quad (39) \end{aligned}$$

**Formulation 1.** Find  $P^{n+1} \in \mathbb{W}(\mathcal{T})$  for all times  $t^{n+1}$  such that

$$B(P^{n+1})(\omega) = B_R(P^{n+1})(\omega) + B_F(P^{n+1})(\omega) = 0 \quad \forall \omega \in \mathbb{W}(\mathcal{T}). \quad (40)$$

---

### 3.3 A Fully-Coupled Formulation of the Euler-Lagrange Equations for $\mathbf{u}$ and $\varphi$

In this section, we present a fully-coupled Euler-Lagrange formulation for  $\mathbf{U}$  and  $\Phi$  (approximating  $\mathbf{u}, \varphi$ ), respectively. We consider a time-discretized system in which time enters through the irreversibility condition. The spatial discretized solution variables are  $\mathbf{U} \in C^1([0, T]; \mathbf{V}_0(\mathcal{T}))$  and  $\Phi \in C^1([0, T]; \mathbb{Z}(\mathcal{T}))$ , where

$$\mathbf{V}_0(\mathcal{T}) := \{W \in C^0(\bar{\Lambda}; \mathbb{R}^d) \mid W = \mathbf{0} \text{ on } \partial\Lambda, W|_{\mathcal{K}} \in \mathbf{Q}^1(\mathcal{K}), \forall \mathcal{K} \in \mathcal{T}\}, \quad (41)$$

$$\mathbb{Z}(\mathcal{T}) := \{Z \in C^0(\bar{\Lambda}; \mathbb{R}) \mid Z^{n+1} \leq Z^n \leq 1, Z|_{\mathcal{K}} \in \mathbf{Q}^1(\mathcal{K}), \forall \mathcal{K} \in \mathcal{T}\}. \quad (42)$$

Moreover, we extrapolate  $\Phi$  (denoted by  $E(\Phi)$ ) in the first terms (i.e., the displacement equation) in Formulation 2 in order to avoid an indefinite Hessian matrix:

$$E(\Phi) = \Phi^{n-2} + \frac{(t - t^{n-1} - t^{n-2})}{(t - t^{n-1}) - (t - t^{n-1} - t^{n-2})} (\Phi^{n-1} - \Phi^{n-2}).$$

This heuristic procedure has been shown to be an efficient and robust method as discussed in [24].

In the following, we denote by  $\mathbf{U}^n, \Phi^n$  the approximation of  $\mathbf{U}(t^n), \Phi(t^n)$  respectively.

**Formulation 2.** *Let us assume that  $P^{n+1}$  is a given approximated pressure at the time  $t^{n+1}$ . Given the initial conditions  $\mathbf{U}^0 := \mathbf{U}(0)$  and  $\Phi^0 := \Phi(0)$  we seek  $\{\mathbf{U}^{n+1}, \Phi^{n+1}\} \in \mathbf{V}_0(\mathcal{T}) \times \mathbb{Z}(\mathcal{T})$  such that*

$$\begin{aligned} A(\mathbf{U}^{n+1}, \Phi^{n+1})(\mathbf{w}, \psi - \Phi^{n+1}) &= \int_{\Lambda} (1-k)(E(\Phi^{n+1})^2 + k)\sigma^+(\mathbf{U}^{n+1}) : e(\mathbf{w}) \, d\mathbf{x} + \int_{\Lambda} \sigma^-(\mathbf{U}^{n+1}) : e(\mathbf{w}) \, d\mathbf{x} \\ &\quad - \int_{\Lambda} (\alpha - 1)E(\Phi^{n+1})^2 P^{n+1} \nabla \cdot \mathbf{w} \, d\mathbf{x} + \int_{\Lambda} E(\Phi^{n+1})^2 \nabla P^{n+1} \cdot \mathbf{w} \, d\mathbf{x} \\ &\quad + (1-k) \int_{\Lambda} \Phi^{n+1} \sigma^+(\mathbf{U}^{n+1}) : e(\mathbf{U}^{n+1}) \cdot (\psi - \Phi^{n+1}) \, d\mathbf{x} \\ &\quad - 2(\alpha - 1) \int_{\Lambda} \Phi^{n+1} P^{n+1} \nabla \cdot \mathbf{U}^{n+1} \cdot (\psi - \Phi^{n+1}) \, d\mathbf{x} + \int_{\Lambda} 2\Phi^{n+1} \nabla P^{n+1} \cdot \mathbf{U}^{n+1} \cdot (\psi - \Phi^{n+1}) \, d\mathbf{x} \\ &- G_c \int_{\Lambda} \frac{1}{\varepsilon} (1 - \Phi^{n+1}) \cdot (\psi - \Phi^{n+1}) \, d\mathbf{x} + G_c \int_{\Lambda} \varepsilon \nabla \Phi^{n+1} \cdot \nabla (\psi - \Phi^{n+1}) \, d\mathbf{x} \geq 0, \quad \forall \{\mathbf{w}, \psi\} \in \mathbf{V}_0(\mathcal{T}) \times \mathbb{Z}(\mathcal{T}). \end{aligned} \quad (43)$$

*This nonlinear variational inequality is solved by combining two Newton methods into one Newton iteration. The first Newton iteration is necessary for solving the nonlinear forward problem  $A(\mathbf{U}^{n+1}, \Phi^{n+1})(\mathbf{w}, \psi) = 0$ . The second iteration is from the constraint  $\Phi^{n+1} \leq \Phi^n$  that is realized via a semi-smooth Newton method that is equivalent to a primal-dual active set strategy. Further details are presented below in Section 3.5 and Algorithm 2.*

**Remark 1** (Further remarks on time-dependencies). *The full system is time-dependent although not all equations contain time derivatives. The pressure equation has a time derivative whereas ‘time’ in the phase field equation enters through the irreversibility constraint. The displacement solution changes in time since the time-dependent variables of the other two equations enter.*

**Remark 2** (Directional derivative). *For later purposes of solving the nonlinear Formulation 2, we compute the Jacobian that is build by computing the directional derivative  $A'(\mathbf{U}^{n+1}, \Phi^{n+1})(\delta\mathbf{U}^{n+1}, \delta\Phi^{n+1}, \mathbf{w}, \psi)$ .*

Then find  $\{\delta\mathbf{U}^{n+1}, \delta\Phi^{n+1}\} \in \mathbf{V}_0(\mathcal{T}) \times \mathbb{Z}(\mathcal{T})$  such that

$$\begin{aligned}
A'(\mathbf{U}^{n+1}, \Phi^{n+1})(\delta\mathbf{U}^{n+1}, \delta\Phi^{n+1}, \mathbf{w}, \psi - \Phi^{n+1}) &= \int_{\Lambda} ((1-k)E(\Phi^{n+1})^2 + k)\sigma^+(\delta\mathbf{U}^{n+1}) : e(\mathbf{w}) \, d\mathbf{x} \\
&\quad + \int_{\Lambda} \sigma^-(\delta\mathbf{U}^{n+1}) : e(\mathbf{w}) \, d\mathbf{x} \\
+ (1-k) \int_{\Lambda} \delta\Phi^{n+1} \sigma^+(\mathbf{U}^{n+1}) : e(\mathbf{U}^{n+1}) \cdot (\psi - \Phi^{n+1}) \, d\mathbf{x} &+ (1-k) \int_{\Lambda} 2\Phi^{n+1} \sigma^+(\delta\mathbf{U}) : e(\mathbf{U}) \cdot (\psi - \Phi^{n+1}) \, d\mathbf{x} \\
- 2(\alpha - 1)P^{n+1} \int_{\Lambda} (\delta\Phi^{n+1} \nabla \cdot \mathbf{U}^{n+1} + \Phi^{n+1} \nabla \cdot \delta\mathbf{U}^{n+1} \cdot (\psi - \Phi^{n+1})) \, d\mathbf{x} & \\
+ 2 \int_{\Lambda} \delta\Phi^{n+1} \nabla P^{n+1} \cdot \mathbf{U}^{n+1} \cdot (\psi - \Phi^{n+1}) \, d\mathbf{x} &+ 2 \int_{\Lambda} \Phi^{n+1} \nabla P^{n+1} \cdot \delta\mathbf{U}^{n+1} \cdot (\psi - \Phi^{n+1}) \, d\mathbf{x} \\
+ G_c \int_{\Lambda} \frac{1}{\varepsilon} \delta\Phi^{n+1} \cdot (\psi - \Phi^{n+1}) \, d\mathbf{x} &+ G_c \int_{\Lambda} \varepsilon \nabla \delta\Phi^{n+1} \cdot \nabla \psi \, d\mathbf{x} \geq 0, \quad \forall \{\mathbf{w}, \psi\} \in \mathbf{V}_0(\mathcal{T}) \times \mathbb{Z}(\mathcal{T}). \quad (44)
\end{aligned}$$

### 3.4 The Fixed Stress Split Iterative Method

#### 3.4.1 Basics

The fixed-stress split iterative method is a standard approach in petroleum engineering for decoupling geomechanics and (multiphase) flow in porous media. The fixed stress split iterative method consists of imposing constant volumetric mean total stress. This means that the stress

$$\sigma_v = \sigma_{v,0} + K_{dr} \nabla \cdot (\mathbf{u} - \mathbf{u}^0) - \alpha(p - p_0), \quad (45)$$

is kept constant at the half-time step. Here the fixed stress coefficient is  $K_{dr} = \frac{3\lambda+2\mu}{3}$ . The iterative process reads as follows: for  $l = 0, 1, 2, \dots$ ,

$$\begin{aligned}
\left(\frac{1}{M} + \frac{\alpha^2}{K_{dr}}\right) \partial_t p^{l+1} + \nabla \cdot \left(\frac{K}{\eta} (\rho_F \mathbf{g} - \nabla p^{l+1})\right) &= -\frac{\alpha}{K_{dr}} \partial_t \sigma_v^l + f \\
&= f - \alpha \nabla \cdot \partial_t \mathbf{u}^l + \frac{\alpha^2}{K_{dr}} \partial_t p^l \quad (46)
\end{aligned}$$

$$-\nabla \cdot \sigma^{por}(\mathbf{u}^{l+1}) + \alpha(\nabla p^{l+1}) = 0 \quad (47)$$

until it meets the convergence criteria. As stopping criteria, we either use simply  $\max\{\|\mathbf{u}^l - \mathbf{u}^{l-1}\|_{L^2(\Lambda)}, \|p^l - p^{l-1}\|_{L^2(\Lambda)}\} \leq TOL_{FS}$  or take the residual with respect to the porosity, e.g. [35].

#### 3.4.2 Fixed-Stress Algorithm for the Discretized Fluid Filled Fracture System

As previously explained, we first solve for the pressure, which is in the case of fractures realized as a pressure diffraction problem:

**Formulation 3.** For each time  $t^{n+1}$  we iterate for  $l = 0, 1, 2, 3, \dots$  to find  $P^{l+1} \in \mathbb{W}$  such that

$$[B(P^{n+1})(\omega)]^{l+1} = [B_R(P^{n+1})(\omega)]^{l+1} + [B_F(P^{n+1})(\omega)]^{l+1} = 0 \quad \forall \omega \in \mathbb{W}(\mathcal{T}),$$

where

$$\begin{aligned}
[B_R(P^{n+1})(\omega)]^{l+1} &:= \chi_R(\Phi^{l+1}) \left( \int_{\Lambda} \rho_R^0 \left( \frac{1}{M} + \frac{3\alpha^2}{3\lambda + 2\mu} \right) \left( \frac{P^{l+1} - P^n}{\delta t} \right) \cdot \omega \, d\mathbf{x} + \int_{\Lambda} \frac{K_R \rho_R^0}{\eta_R} (\nabla P^{l+1} - \rho_R^0 \mathbf{g}) \nabla \omega \, d\mathbf{x} \right. \\
&\quad \left. + \int_{\Lambda} \alpha \nabla \cdot \left( \frac{\mathbf{U}^l - \mathbf{U}^n}{\delta t} \right) \cdot \omega \, d\mathbf{x} - \int_{\Lambda} \left( \frac{3\alpha^2}{3\lambda + 2\mu} \right) \left( \frac{P^l - P^n}{\delta t} \right) \omega \, d\mathbf{x} - \int_{\Lambda} q_R \omega \, d\mathbf{x} \right), \quad \forall \omega \in \mathbb{W}(\mathcal{T}), \quad (48)
\end{aligned}$$

---

**Algorithm 1** Fixed-stress for phase field fluid-filled fractures in porous media

---

At each time  $t^n$

**repeat**

Solve two-field fixed-stress (inner loop).

Solve the (linear) pressure diffusion Formulation 3.

Solve the (nonlinear) fully-coupled elasticity phase field Formulation 4 using Algorithm 2.

**until** Stopping criterion

$$\max\{\|P^l - P^{l-1}\|, \|\mathbf{U}^l - \mathbf{U}^{l-1}\|, \|\Phi^l - \Phi^{l-1}\|\} \leq \text{TOL}_{\text{FS}}, \quad \text{TOL}_{\text{FS}} > 0$$

for fixed-stress split is satisfied.

Set:  $(P^n, \mathbf{U}^n, \Phi^n) := (P^l, \mathbf{U}^l, \Phi^l)$ .

Increment  $t^n \rightarrow t^{n+1}$ .

---

$$[B_F(P^{n+1})(\omega)]^{l+1} := \chi_F(\Phi^{l+1}) \left( \int_{\Lambda} \rho_F^0 c_F \left( \frac{P^{l+1} - P^n}{\delta t} \right) \omega \, d\mathbf{x} + \int_{\Lambda} \frac{K_F \rho_F^0}{\eta_F} (\nabla P^{l+1} - \rho_F^0 \mathbf{g}) \nabla \omega \, d\mathbf{x} - \int_{\Lambda} (q_F - q_L) \omega \, d\mathbf{x} \right), \quad \forall \omega \in \mathbb{W}(\mathcal{T}). \quad (49)$$

Then, we solve for the displacement-phase-field inequality:

**Formulation 4.** We solve for the displacements  $\mathbf{U}^{l+1} \in \mathbf{V}_0(\mathcal{T})$  and the phase field  $\Phi^{l+1} \in \mathbb{Z}(\mathcal{T})$  such that:

$$A(\mathbf{U}^{l+1}, \Phi^{l+1})(\mathbf{w}, \psi - \Phi^{l+1}) \geq 0 \quad \forall \{\mathbf{w}, \psi\} \in \mathbf{V}_0(\mathcal{T}) \times \mathbb{Z}(\mathcal{T}), \quad (50)$$

where

$$\begin{aligned} A(\mathbf{U}^{l+1}, \Phi^{l+1})(\mathbf{w}, \psi - \Phi^{l+1}) &= \int_{\Lambda} ((1-k)(E(\Phi^{l+1})^2 + k)\sigma^+(\mathbf{U}^{l+1}) : e(\mathbf{w}) \, d\mathbf{x} + \int_{\Lambda} \sigma^-(\mathbf{U}^{l+1}) : e(\mathbf{w}) \, d\mathbf{x} \\ &- \int_{\Lambda} (\alpha-1)E(\Phi^{l+1})^2 P^{l+1} \nabla \cdot \mathbf{w} \, d\mathbf{x} + \int_{\Lambda} E(\Phi^{l+1})^2 \nabla P^{l+1} \cdot \mathbf{w} \, d\mathbf{x} + (1-k) \int_{\Lambda} \Phi^{l+1} \sigma^+(\mathbf{U}^{l+1}) : e(\mathbf{U}^{l+1})(\psi - \Phi^{l+1}) \, d\mathbf{x} \\ &- 2(\alpha-1) \int_{\Lambda} \Phi^{l+1} P^{l+1} \nabla \cdot \mathbf{U}^{l+1} (\psi - \Phi^{l+1}) \, d\mathbf{x} + \int_{\Lambda} 2\Phi^{l+1} \nabla P^{l+1} \cdot \mathbf{U}^{l+1} (\psi - \Phi^{l+1}) \, d\mathbf{x} \\ &- G_c \int_{\Lambda} \frac{1}{\varepsilon} (1 - \Phi^{l+1})(\psi - \Phi^{l+1}) \, d\mathbf{x} + G_c \int_{\Lambda} \varepsilon \nabla \Phi^{l+1} \cdot \nabla (\psi - \Phi^{l+1}) \, d\mathbf{x} \geq 0, \quad \forall \{\mathbf{w}, \psi\} \in \mathbf{V}_0(\mathcal{T}) \times \mathbb{Z}(\mathcal{T}). \end{aligned} \quad (51)$$

**Remark 3** (Stopping criterion). The iteration between Formulation 3 and 4 is completed if

$$\max\{\|\mathbf{U}^{l+1} - \mathbf{U}^l\|_{L^2(\Lambda)}, \|P^{l+1} - P^l\|_{L^2(\Lambda)}, \|\Phi^{l+1} - \Phi^l\|_{L^2(\Lambda)}\} < \text{TOL}_{\text{FS}}.$$

Then we set

$$P^{n+1} = P^{l+1}, \quad \Phi^{n+1} = \Phi^{l+1}, \quad \mathbf{U}^{n+1} = \mathbf{U}^{l+1}.$$

Here we choose  $\text{TOL}_{\text{FS}} = 10^{-4}$ .

**Remark 4.** For pressurized fractures, no fixed-stress splitting is necessary, since the pressure (flow) is a given right-hand-side quantity (e.g.  $\alpha = 0$  and  $p = \text{const}$ ) and only for fluid filled fractures (e.g.  $\alpha = 1$ ), the fixed stress iteration has to be employed.

---

### 3.5 Solution Algorithm for Solving the Displacement-Phase-Field Problem (Formulation 4)

The nonlinear variational inequality presented in Formulation 2 (i.e., Formulation 4, respectively) is solved with Newton's method in which two nonlinear iterations are combined. The first Newton iteration is required to solve the nonlinear forward problem and the second (semi-smooth) Newton method is a realization of a primal-dual active set strategy to treat the crack irreversibility constraint. The resulting scheme is outlined in Algorithm 2. In order to enhance the convergence radius, a standard backtracking line search algorithm is employed. Within Newton's method, the linear equations, are solved with GMRES with diagonal block-preconditioning from Trilinos [25]. Algorithm 1 presents the overall fixed-stress phase field approach for fluid filled fractures in which the geomechanics-phase-field system is coupled to the pressure diffusion problem.

---

**Algorithm 2** Primal-dual active set for pressurized fractures ([24])

---

At a given time  $t^n$  compute for each Newton step  $k = 0, 1, 2, \dots$

**repeat**

Assemble residual  $R(\mathbf{U}_k; \Phi_k)$  for Formulation 2.

Compute active set  $\mathcal{A}_k = \{i \mid (B^{-1})_{ii}(R_k)_i + c(\delta\Phi_k)_i > 0\}$ , where  $(B)_{ii}$  is a diagonal mass matrix (see [26]).

Assemble matrix  $G = A'(\mathbf{U}, \Phi)(\delta\mathbf{U}, \delta\Phi, \mathbf{w}, \psi)$  and right-hand side  $F = -A(\mathbf{U}, \Phi)(\mathbf{w}, \psi)$ .

Eliminate rows and columns in  $\mathcal{A}_k$  from  $A'(\mathbf{U}, \Phi)(\delta\mathbf{U}, \delta\Phi, \mathbf{w}, \psi)$  and  $A(\mathbf{U}, \Phi)(\mathbf{w}, \psi)$ .

The reduced systems are denoted with  $\tilde{A}'(\mathbf{U}, \Phi)(\delta\mathbf{U}, \delta\Phi, \mathbf{w}, \psi)$  and  $\tilde{A}(\mathbf{U}, \Phi)(\mathbf{w}, \psi)$ , respectively.

Solve the linear system

$$\tilde{A}'(\mathbf{U}_k, \Phi_k)(\delta\mathbf{U}_k, \delta\Phi_k, \mathbf{w}, \psi) = -\tilde{A}(\mathbf{U}_k, \Phi_k)(\mathbf{w}, \psi), \quad \forall \{\mathbf{w}, \psi\} \in \mathbf{V}_0(\mathcal{T}) \times \mathbb{Z}(\mathcal{T}).$$

Find a step size  $0 < \gamma \leq 1$  using line search (see Remark 5) to obtain

$$\mathbf{U}_{k+1} = \mathbf{U}_k + \gamma\delta\mathbf{U}_k, \quad \Phi_{k+1} = \Phi_k + \gamma\delta\Phi_k \tag{52}$$

with  $\tilde{R}(\mathbf{U}_{k+1}; \Phi_{k+1}) < \tilde{R}(\mathbf{U}_k; \Phi_k)$ .

**until** Stopping criterium:

$$\mathcal{A}_{k+1} = \mathcal{A}_k \quad \text{and} \quad \tilde{R}(\mathbf{U}_k) < \text{TOL}.$$


---

**Remark 5** (Line search). *A crucial role for (highly) nonlinear problems includes the appropriate determination of  $\gamma$ . A simple strategy is to modify the update step in (52) as follows: For given  $\gamma \in (0, 1)$  (in our numerical tests, we choose  $\gamma = 0.6$ ) determine the minimal  $l^* \in \mathbb{N}$  via  $l = 0, 1, \dots, N_l$ , such that*

$$\begin{aligned} R(\mathbf{U}_{k+1,l}^h) &< R(\mathbf{U}_{k,l}^h), \\ \mathbf{U}_{k+1,l}^h &= \mathbf{U}_{k+1}^h + \gamma^l \delta\mathbf{U}_k^h. \end{aligned}$$

For the minimal  $l$ , we set

$$\mathbf{U}_{k+1}^h := \mathbf{U}_{k+1,l^*}^h.$$

In this context, the nonlinear residual  $R(\cdot)$  is defined as

$$R(\mathbf{U}^h) := \max_i \left\{ A(\mathbf{U}^h)(\Psi_i) - \hat{F}(\Psi_i) \right\} \quad \forall \mathbf{U}^h = \{\mathbf{w}, \psi\} \in \mathbf{V}_0(\mathcal{T}) \times \mathbb{Z}(\mathcal{T}),$$

---

where  $\{\Psi_i\}$  denotes the nodal basis of  $\mathbf{V}_0(\mathcal{T}) \times \mathbb{Z}(\mathcal{T})$ . This algorithm works quite well for our problems and is applied to both the nonlinear forward model and the semi-smooth Newton method to realize the primal-dual active set.

### 3.6 Adaptive Mesh Refinement along the Fracture

A crucial issue in phase-field methods is the resolution of the interface (i.e., here the fracture) such that  $\varepsilon > h$  is guaranteed. Local mesh refinement is a well-known technique to only refining the mesh in regions where high accuracy of the solution or resolution of certain features is needed. However, in fracture propagation the path of the fracture is (in most cases) unknown and it is a priori not clear where mesh refinement should be carried out. Moreover,  $\varepsilon$  is only to be required small in the crack region

$$\Phi(\mathbf{x}_K, t) \leq C_R, \quad (53)$$

where  $\mathbf{x}_K$  is the barycenter of a cell  $K$ . This enables us to choose a priori a small  $\varepsilon$  that ensures the condition  $\varepsilon > h$  locally (in the crack region). The challenge is that the crack might grow into regions where  $\varepsilon > h$  is violated. For two-dimensional applications a solution in terms of predictor-corrector adaptivity has been developed in [24]. This technique has been extended in the present paper to three-dimensional applications:

- First, the future crack path is first predicted by solving once the system;
- Then, the mesh is refined in the predicted region using as refinement indicator the phase-field variable itself with a threshold  $C_R$  such that all cells refined in which  $\Phi(\mathbf{x}_K, t) \leq C_R$ ;
- Next, the old time step solution is taken again and the system is solved once more but now on the new refined mesh, which now satisfies  $\varepsilon > h$ .

Despite solving the system twice from time to time, this method has been shown to work very efficiently for 2D applications. The key question remains how this idea performs for 3D problems is still open, and will be studied for some test cases in the numerical section.

Of course in our applications  $\varepsilon$  is chosen reasonably small such that 3–5 predictor steps are necessary at most in order to satisfy the criterion  $\varepsilon > h$ . In particular, the smallest  $\varepsilon$  is chosen at the beginning of the computation and this choice is kept during the entire computation.

## 4 Numerical Experiments

In this final section, we present numerical studies that demonstrate the capabilities of our method. All examples are computed with the open-source finite element package deal.II [7]. In particular, the three dimensional implementation of Algorithm 2 is an extension of the two dimensional MPI-parallel framework proposed in [24].

In the beginning, we start from illustrating pressurized fracture propagation ( $\alpha = 0$ ) examples for studying the performance of our algorithm by comparing with analytical and physical benchmark problems. Thus, in the first example, we compute a test with increasing pressure and verify the volume-radius relationship derived by Sneddon/Lowengrub's theory [49]. Then, well known multiple parallel fractures interacting in the stress shadowing effect are presented in Section 4.2 and joining and branching fractures in homogeneous and heterogeneous media are studied in Section 4.3. To date, detailed studies with respect to mesh dependencies and computational cost are missing in the literatures because global mesh refinement becomes prohibitive for such configurations because of

CPU times. In this paper, those studies are accomplished by using parallel computing and adaptive mesh refinement. Thus, we investigate these two aspects in the first three examples for pressurized fractures. We emphasize that we restrict our attention to  $h$ -refinement while keeping  $\varepsilon$  fixed. The task of letting  $h$  and  $\varepsilon$  going to zero is non-trivial to show. We also provide the examples in Section 4.4 - 4.6 to emphasize our fluid filled fracture model with  $\alpha = 1$ . In the fifth and sixth example, we concentrate on other aspects that are related specifically to reservoir engineering and towards realistic configurations; namely we present a well model and study dependence of the crack path on the critical energy release rate  $G_c$ .

We briefly describe the fixed parameters and boundary conditions assumed in all of our computational results. The initial thickness of fractures is set to  $\varepsilon = 2h_{\min}$  as illustrated on Figure 3b, where  $h_{\min}$  is the minimum mesh size. We assume  $\mathbf{u} = \mathbf{0}$  and homogeneous Neumann boundary condition on  $\partial\Lambda$  for the pressure. In addition, we set the regularization parameter  $k = 10^{-10} \times h_{\min}$ , and all contour figures are plotted for  $\varphi \leq 0.1$  with given  $C_R = 0.8$ .

#### 4.1 Sneddon's Theory with Step-Wise Increasing Pressure

In this example, we consider a standard benchmark setting for a pressurized penny-shape fracture in an elastic medium. Here, the theory of Sneddon and Lowengrub [49] applies. Findings for a fixed pressurized fracture using variational and phase field methods have been presented for instance in [12, 52]. We now extend Sneddon's benchmark for the case of a propagating fracture in order to study the evolution of radius, volume and pressure as it has been recently done in [12, 23].

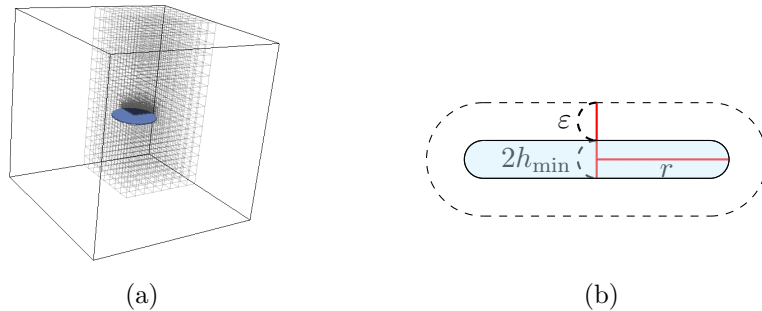


Figure 3: Example 4.1: (a) Initial penny shape crack is centered at (5 m, 5 m, 5 m) on  $y = 5$  m–plane with the mesh refinement. (b) Illustrates the thickness of the fracture ( $2h_{\min}$ ), radius of the fracture ( $r$ ) and phase field parameter ( $\varepsilon$ )

In the computational domain  $\Lambda = (0, 10 \text{ m})^3$ , the initial penny shape crack is centered at (5 m, 5 m, 5 m) on  $y = 5$  m–plane and we refine around the crack ( $C_R = 0.8$ ); see Figure 3a for the setup. We perform 8 computations with different radii  $r = 1, 1.25, 1.375, 1.5, 1.625, 1.75, 1.875$ , and 2.0 m. Each growing radius corresponds to different values ( $G_c$ ) by

$$G_c = \frac{4}{\pi E'} p^2 r, \quad (54)$$

where  $E' = E/(1 - \nu^2)$  and  $G_c = 1$ . The mechanical parameters are Young's modulus and Poisson's ratio  $E = 1.0$  and  $\nu = 0.2$ . The relation to the Lamé coefficients  $G$  and  $\lambda$  is given by standard relations.

For each step, the constant pressure opens the initial crack with the different values of  $r$  and  $G_c$ , and afterwards we measure the crack opening displacement. The theory of measuring the crack opening

---

$r$	1.0	1.25	1.375	1.5	1.625	1.75	1.875	2.0
$p$	0.9908	0.8862	0.8450	0.8090	0.7773	0.7490	0.7236	0.7006

Table 1: The value of pressure ( $p$ ) related to the radius ( $r$ ).

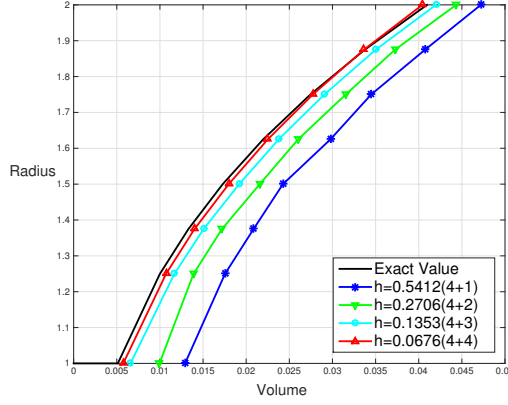


Figure 4: Example 4.1: We observe the convergence of the value  $V_N$  (58) under the spatial mesh refinement.

displacement (COD) in 3D at the center ( $x = 5$ ) is presented in [49] and the numerical approximation is given as

$$\mathbf{u}_y = \frac{4(1 - \nu^2)pr}{\pi E} \approx \frac{1}{2}[\mathbf{u} \cdot \mathbf{n}^+]. \quad (55)$$

We take  $\varepsilon = 2h_{\min}$ , and we approximate the COD value at the point  $(5, 5 + h_{\min}, 5)$ ; see Figure 3b for the details.

Figure 4 shows the relation between the volume and the radius of the crack. These tests are computed in a quasi-stationary manner: that is, we solve several pseudo-time steps until the residual  $< \text{TOL} = 10^{-5}$  is reached. The theoretical relation between the radius and volume is given in [12, 23] and is based on [49]. In the following, we recapitulate the principal ideas: From the volume of an ellipsoid,

$$V = \frac{4}{3}\pi a_1 a_2 a_3,$$

with  $a_1 = a_2 = r$  and  $a_3 = \mathbf{u}_y$ , we obtain

$$V = \frac{16}{3E'}pr^3,$$

by (55). From (54), we rewrite the pressure by

$$p = \sqrt{\frac{G_c \pi E'}{4r}}, \quad (56)$$

then we get the relationship

$$V = \sqrt{\frac{64G_c \pi r^5}{9E'}}. \quad (57)$$

The relation between the radius and pressure used in the test is presented on the Table 1. To compare with our numerical computations, we approximate the volume  $V$

$$V \approx V_N := \frac{4}{3}\pi r^2 \mathbf{u}_y, \quad (58)$$

and compare  $V_N$  with (57). The result is given at the Figure 4.

## 4.2 Multiple Parallel Fractures

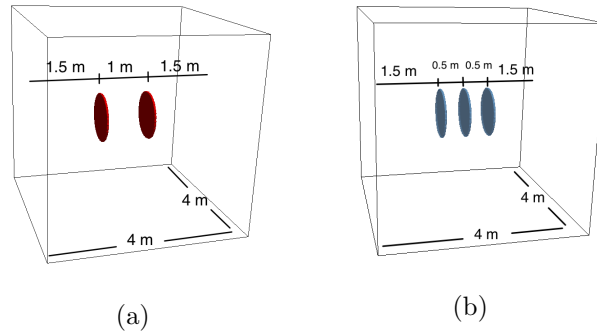


Figure 5: Initial setup for Section 4.2.1 and Section 4.2.2 in the domain  $\Lambda = (0, 4\text{ m})^3$ . (a) Two initial parallel fractures. The radius of both initial penny shape fractures is  $r = 0.5\text{ m}$  and they are centered at  $x = 1.5\text{ m}$  and  $x = 2.5\text{ m}$ -plane, respectively. (b) Three initial parallel fractures. The radius of all three penny shape initial fractures is  $0.5\text{ m}$  and they are centered at  $x = 1.5\text{ m}$ ,  $2\text{ m}$  and  $x = 2.5\text{ m}$ -plane, respectively.

In this section, we present and study the interaction between multiple parallel fractures in three dimensional domains to verify our algorithm. Here, we study that close enough parallel fractures interact with each other under the stress shadowing effect, see [13, 15, 41, 54].

### 4.2.1 Two Parallel Fractures

In the domain  $\Lambda = (0, 4\text{ m})^3$ , we set two initial penny shape fractures as shown in the Figure 5a. The left fracture is centered at  $(1.5\text{ m}, 2\text{ m}, 2\text{ m})$  with radius  $r = 1\text{ m}$  on  $x = 1.5\text{ m}$ -plane and the right fracture is centered at  $(2.5\text{ m}, 2\text{ m}, 2\text{ m})$  with radius  $r = 0.5\text{ m}$  on  $x = 2.5\text{ m}$ -plane. Here  $G_c = 1.0\text{ Pa m}$  and Lamé coefficients are given as  $G = 4.2 \times 10^7\text{ Pa}$  and  $\lambda = 2.8 \times 10^7\text{ Pa}$ . The fractures grow by a given constant pressure in space and linearly increasing in time;  $p = t \times 5 \times 10^4\text{ Pa}$ , where  $t$  is the current time. The discretization parameters are  $\delta t = 0.005\text{ s}$  and  $h_{\min} = 0.027\text{ m}$ .

As we observe in the Figure 6, if the distance between the fractures is sufficiently close, then they influence each other via their stress fields, often referred to by engineers as the stress shadowing effect. The leading edges of the fractures start to grow by curving out from the initial cracks. The interaction between the fractures increases when the fractures become larger. Similar studies with analogous findings have been carried out in [13, 15, 41, 54].

To illustrate the performance of the algorithm, we computed the above example by using fifteen Intel(R) Xeon(R) CPU X5670 @ 2.93GHz processors. The average wall clock time for each time step including predictor-corrector adaptive step is approximately  $826.078\text{ s}$  and the computation requires 74 time steps plus 71 additional predictor-corrector adaptive iterations. Consequently, the total wall

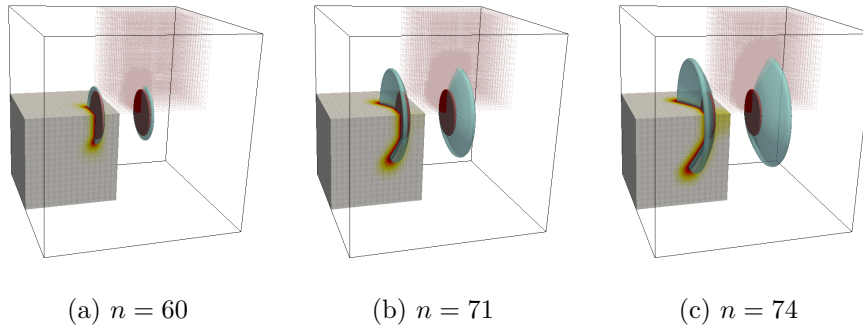


Figure 6: Example 4.2.1: Propagation of two parallel fractures for increasing pressure for each time step  $n$ . For each figure, the inner bold penny shape fractures indicate the initial two parallel fractures and red wire lines illustrates the part of adaptive meshes. We observe the stress-shadowing effect that causes the two fractures to curve away.

clock time for this computation was approximately 17 hours. The space discretization is adaptively modified after each time step and the maximum number of total degrees of freedom is 4,074,532 and the minimum number is 318,846. The average wall clock time per degree of freedom per time step is approximately  $4.929 \times 10^{-5} s$ .

#### 4.2.2 Three Multiple Parallel Fractures

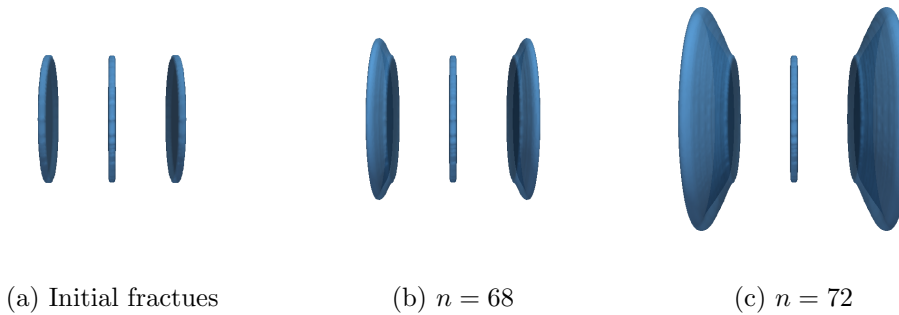


Figure 7: Example 4.2.2: Growth of three parallel fractures for each time step  $n$ .

Here we increase the number of fractures from two to three, but all other mechanical and numerical constants are the same as in the previous example. Between the two initial fractures in the Figure 5a, we add an additional fracture at  $x = 2$  m-plane with the same radius as the others; we refer to Figure 5b for the setup. Following Figure 7 shows the propagation of the fractures for each time step. The middle fracture does not grow as pressure is increased because of the stress-shadowing effect.

In addition, we perform another test by enlarging the radius of the initial fracture only in the middle (on  $x = 2$  m-plane). Here, the radius of the middle fracture is now  $r = 0.75$  m. In this case, the stress-shadowing effect from the middle fracture prevents the growth of the two other fractures as it can be observed in Figure 8.

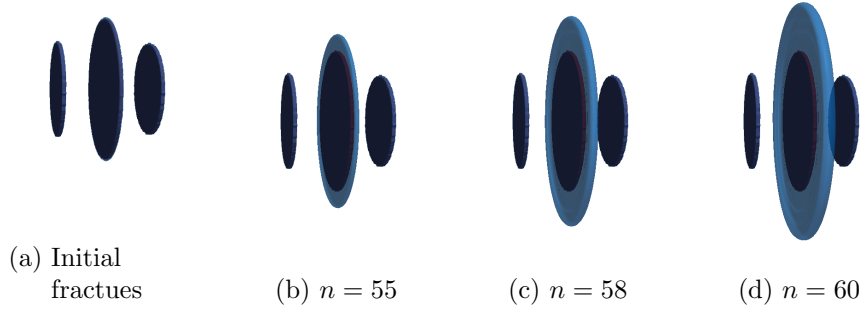


Figure 8: Example 4.2.2: Growth of three parallel fractures with larger initial radius in the middle for each time step  $n$ . The darker region inside indicate the initial fractures. The larger middle fracture grows faster than the others.

### 4.3 Two Perpendicular Fractures in Homogeneous and Heterogeneous Media with Locally Refined Meshes

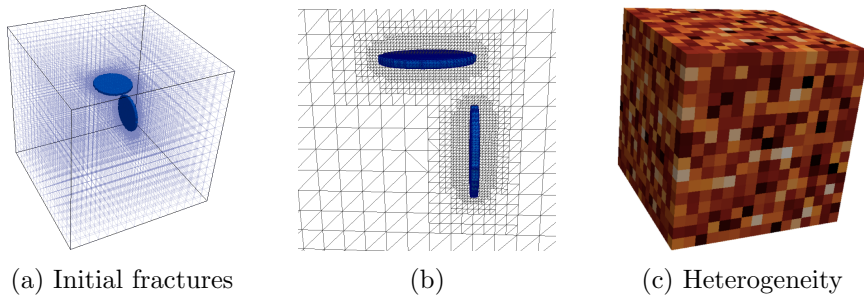


Figure 9: Example 4.3: Initial setup for two perpendicular fractures in the locally refined three dimensional domain  $\Lambda = (0, 4 \text{ m})^3$ . (b) Cut through the  $z = 2 \text{ m}$ -plane to observe the initially refined meshes near the fractures.(c) Random heterogeneity by Young's modulus  $E$  value range of the shale rock region;  $E \in [1 \text{ GPa}, 10 \text{ GPa}]$ .

In this section, we predict two initial fractures in arbitrary positions propagating by a given increasing pressure. We emphasize the joining and branching of the fractures in 3D domain with the locally refined meshes. We also observe non-planar fractures especially in heterogeneous media.

Figure 9 presents the initial setup with hanging nodes for the multiple fractures on the locally refined domain  $\Lambda = (0, 4 \text{ m})^3$ . The top penny shape fracture is centered at  $(2 \text{ m}, 3 \text{ m}, 2 \text{ m})$  with radius  $r = 0.5 \text{ m}$  in  $y = 3 \text{ m}$ -plane and the bottom fracture is centered at  $(2.5 \text{ m}, 2 \text{ m}, 2 \text{ m})$  with radius  $r = 0.5 \text{ m}$  in  $x = 2.5 \text{ m}$ -plane. The mechanical parameters are  $\nu = 0.2$  and  $E = 10^4 \text{ Pa}$  for the homogeneous domain but  $E \in [1 \text{ GPa}, 10 \text{ GPa}]$  for the heterogeneous domain, see Figure 9c [53]. Here the pressure is given by  $p = t \times 10^3 \text{ Pa}$  and  $p = t \times 1 \text{ MPa}$ , for homogeneous and heterogeneous domain, respectively. The discretization parameters are  $\delta t = 0.01$  and  $h_{\min} = 0.054 \text{ m}$ .

The following Figures 10 and 13 show each time step  $n$  of non planar fractures propagating with joining and branching in homogeneous and heterogeneous media, respectively. We take detailed snapshots for joining and branching of fractures; see Figure 11a- 11b. Those are automatically captured by the proposed phase field model.

In Figure 11c, the bulk and crack energies are presented in time. Recall that the bulk energy and

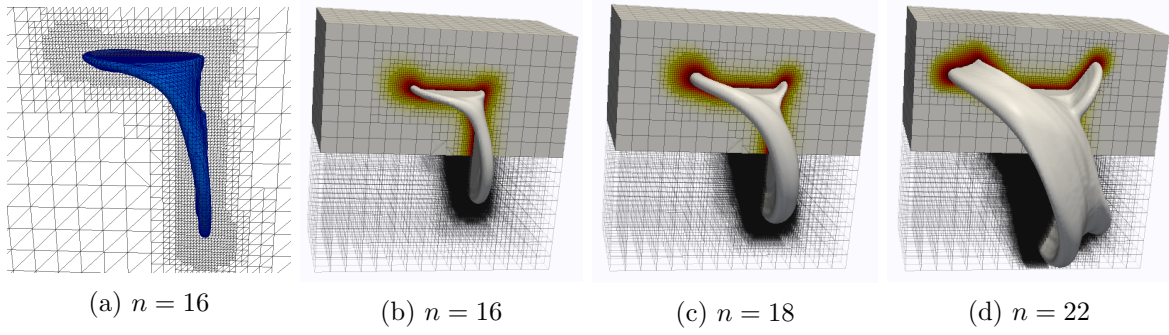


Figure 10: Example 4.3: Multiple fracture propagation in homogeneous media in 3D. Two fractures first join and later branch. Employing the predictor-corrector mesh adaptivity technique, the locally refined mesh follows the crack patterns. This strategy allows for high resolution of  $\varepsilon$  around the crack pattern but keeps the overall computational cost reasonable since the number of degrees of freedom grows with the cracks.

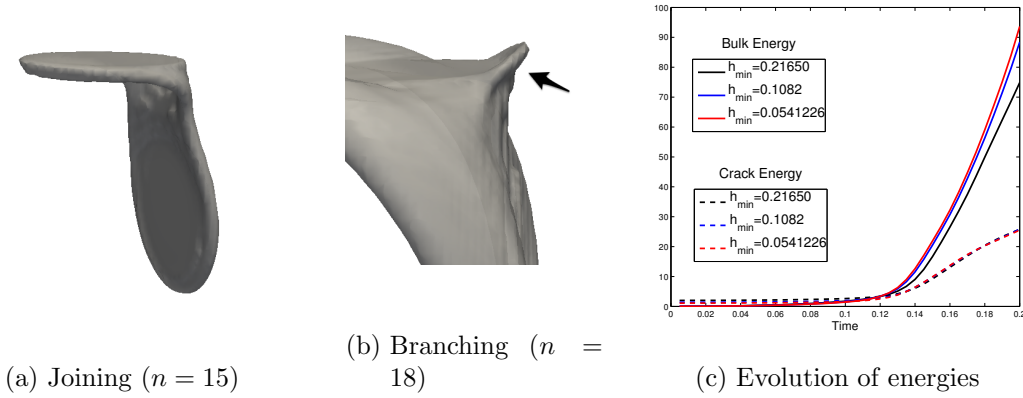


Figure 11: Example 4.3: Detailed snapshots of the areas where the cracks are (a) joining of two fractures at  $n = 15$  and (b) strats branching after joining at  $n = 18$ . (c) Evolution of bulk and crack energies. The crack energy (dotted line) starts increasing when the two fractures start growing at  $n = 10$  (equal to  $t = 0.1$ ). The bulk energy (solid line) remains increasing even for propagating fractures since the applied pressure is still increasing.

the crack energy are given by

$$E_{Bulk} = \frac{1}{2} \int_{\Lambda} ((1 - k)\varphi^2 + k)\sigma(\mathbf{u}) : e(\mathbf{u}) \, d\mathbf{x}, \quad \text{and} \quad E_{Crack} = \frac{G_c}{2} \int_{\Lambda} \left( \frac{1}{\varepsilon}(1 - \varphi^2) + \varepsilon|\nabla\varphi|^2 \right) \, d\mathbf{x}.$$

We observe that the crack energy remains constant while the cracks are not growing and this energy increases for growing fractures. In addition, we fix the  $\varepsilon = 0.2165$  but refine  $h_{\min}$  ( $= 0.2165, 0.1082$  and  $0.0541$ ) and observe the spatial convergence of both energies with respect to  $h_{\min}$ .

We emphasize the predictor-corrector mesh refinement in the Figure 9b and Figure 10a. Finally, in Table 2, we study the number of predictor-corrector mesh refinement iterations for each different time step. For total 22 time steps, the mesh was changed 38, 50 and 52 times in the test with  $C_R = 0.4, 0.6$  and  $0.8$ , respectively. We see more predictor-corrector iteration steps for larger  $C_R$  values, which is clear since we mark more cells in a larger area near the fracture to refine. Not only the iteration numbers, but also larger  $C_R$  results in more degrees of freedom. For instance, the maximum numbers

for total degrees of freedom are 1449500, 1880008, and 2394108 for  $C_R = 0.4, 0.6$  and  $0.8$ , respectively. However, the evolution of the energies are compared to be similar; see Figure 12.

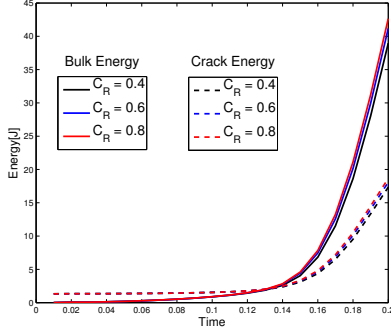


Figure 12: Example 4.3: Evolution of bulk and crack energies with different  $C_R$  values are similar.

Time steps ( $n$ )	Predictor-Corrector iterations		
	$C_R = 0.4$	$C_R = 0.6$	$C_R = 0.8$
i) 1 - 9	5	15	16
ii) 10 - 15	13	15	15
iii) 16 - 22	20	20	21

Table 2: Example 4.3: Display of the average number of predictor-corrector iterations for different time intervals: i) before the fractures grow, ii) before it joins, and iii) while branching. Each column represents a different value of the threshold value  $C_R$ .

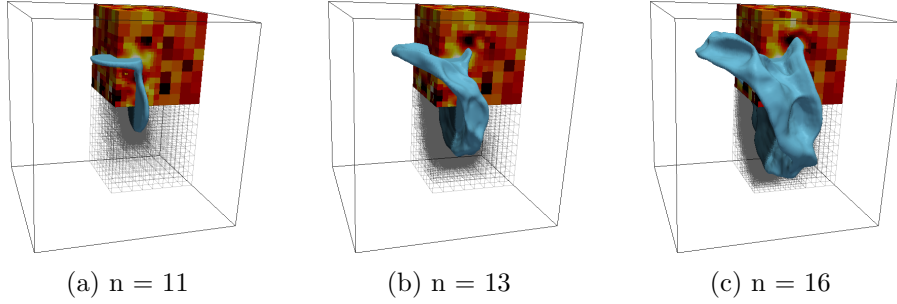


Figure 13: Example 4.3 in heterogeneous media: Sequence of snapshots of fractures propagating at each time step number  $n$  in three dimensional heterogeneous media. Both fractures grow non-planarly, then they join at  $n = 11$  and start branching at  $n = 13$ . In these examples, we observe non-planar fracture propagation.

#### 4.4 Fluid Filled Fractures

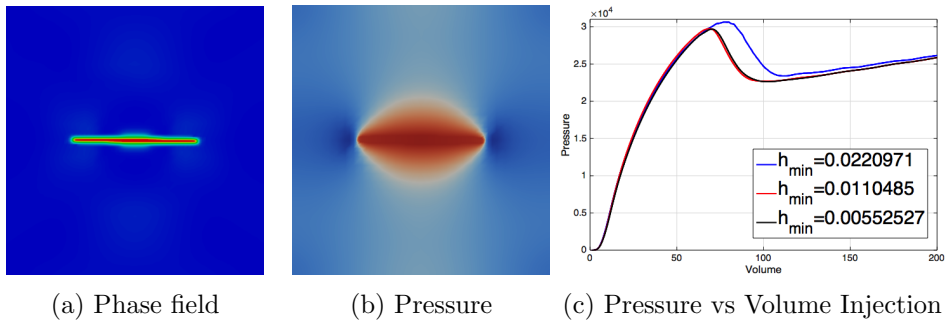


Figure 14: Example 4.4: (a) Phase field, (b) the pressure value at  $t = 1$ , and (c) the average pressure in the fracture by volume injection.

From this section on, we study the fluid filled fracture propagation examples ( $\alpha = 1$ ). The pressure

diffraction problem is fully coupled with the displacement-phase field system as outlined in Section 3.5 and Algorithm 1.

First, the initial fracture is centered at  $(2\text{ m}, 2\text{ m})$  with the length  $l = 0.25\text{ m}$  in the two dimensional domain  $\Lambda = (0, 4\text{ m})^2$ . The mechanical parameters are  $\nu = 0.2$  and  $E = 10^8\text{ Pa}$  for the homogeneous domain. The fluid is injected at the center of the fracture with the constant volume rate of  $q_F = 200$  for point source injection and  $q_L = 0$ . The fluid parameters are given as  $\mu_F = \mu_R = 1 \times 10^{-3}\text{ Ns/m}^2$ ,  $\rho_R = \rho_F = 1000\text{ kg/m}^3$ . Also other parameters are  $K_R = 1 \times 10^{-12}$ ,  $\mathbf{g} = 0$ ,  $c_F = 1 \times 10^{-8}$ , and the Biot modulus is  $M = 2.5 \times 10^8$ . Figure 14a and 14b illustrate the phase field and the pressure values at the final time  $t = 1$ . Here  $h_{\min} = 0.022\text{ m}$  and the time step is  $\delta t = 0.01\text{ s}$ . The pressure increases until the fracture starts propagating and then drops as expected from previous studies; see Figure 14c. In addition, we fix the phase field parameter as  $\varepsilon = 0.045$  and the initial thickness of the fracture as  $0.02\text{ m}$  then refine  $h_{\min} = 0.022, 0.011, 0.0055\text{ m}$  to see the convergence of the average pressure value in the fracture with respect to  $h_{\min}$ .

In the three dimensional domain  $\Lambda = (0, 4\text{ m})^3$ , the initial penny shape fracture is centered at  $(2\text{ m}, 2\text{ m}, 2\text{ m})$  on  $y = 2\text{ m}$ -plane with the radius  $r = 0.25\text{ m}$ . The fluid is injected at the center of the fracture and all the parameters are the same as previous two dimensional example. Here  $h_{\min} = 0.05\text{ m}$  and the time step is  $\delta t = 0.01\text{ s}$ .

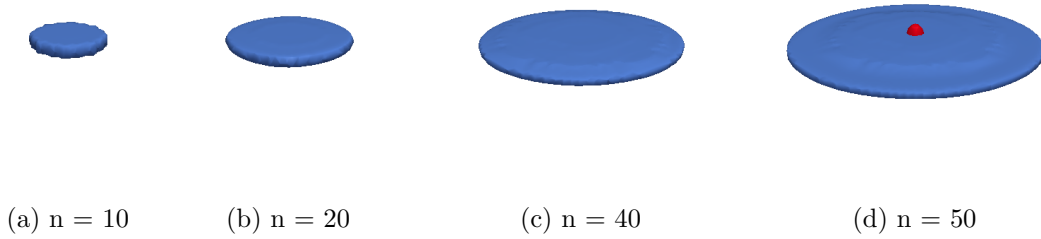


Figure 15: Example 4.4: Sequence of snapshots of fractures propagating at each time step number  $n$  in three dimensional homogeneous media. (d) The red dot in the middle of the fracture indicates the injection well point.

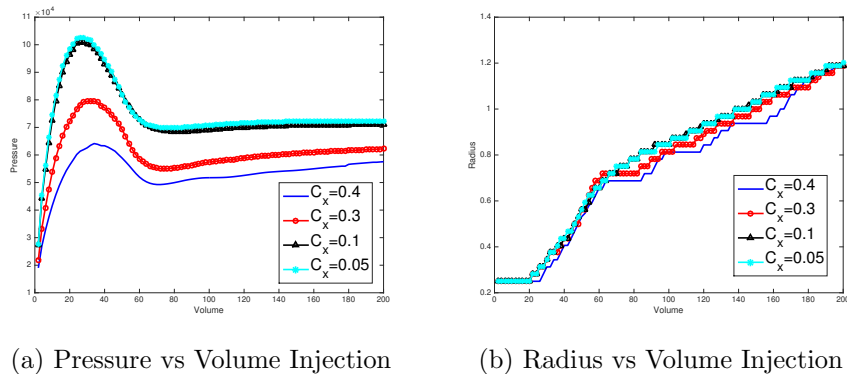


Figure 16: Example 4.4: Pressure increases until the fracture starts to propagate and then drops.

Figure 15 illustrates each step of the fracture propagation by the injection of fluid. In addition, we vary the  $c_x$  values for the pressure diffraction system to study the differences. In Figure 16 the

maximum pressure in the fracture and the radius of the fracture is plotted by the fluid injection volume. In this example, we use (14) to split the stress; thus the energy degradation only acts on the tensile part and additional fractures do not develop because of the compression.

#### 4.5 Multiple Fluid Filled Fractures Growing From a Well Bore

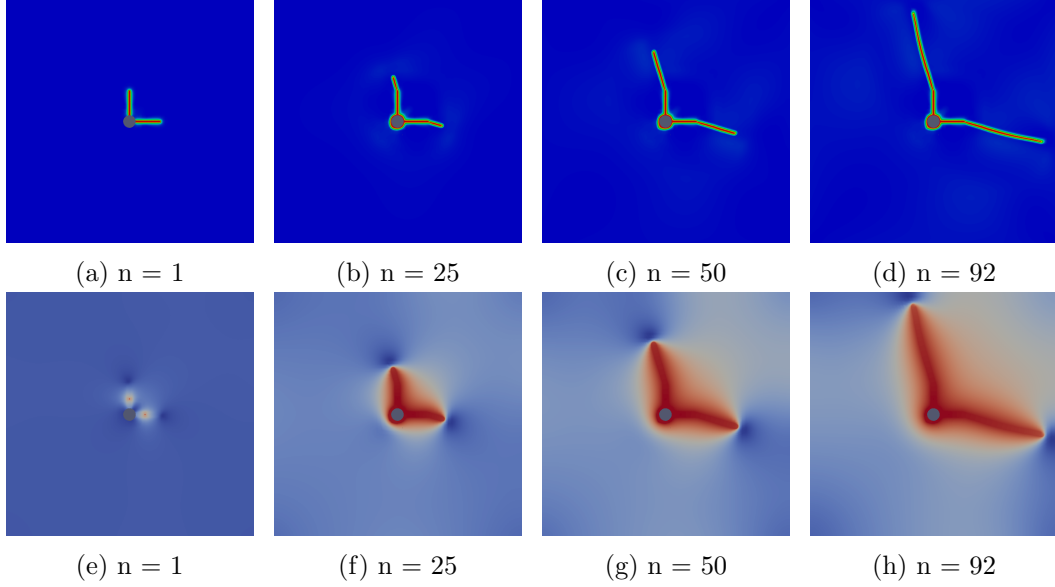


Figure 17: Example 4.5: (a)-(d) Sequence of snapshots of fluid filled fractures propagating, and (e)-(h) pressure distribution for each time step number  $n$ .

The computational domain is given as  $\Lambda = (-2\text{ m}, 2\text{ m})^2 \setminus \mathbb{O}$ , where  $\mathbb{O} := \{\mathbf{x} \mid |\mathbf{x} - \mathbf{c}| \leq r\}$  is the circle with the center  $\mathbf{c} = (0\text{ m}, 0\text{ m})$  and the radius  $r = 0.1\text{ m}$ , which represents the well bore. The initial fractures are positioned at  $(0 - h_{\min}, 0 + h_{\min}) \times (0.1, 0.5)$  and  $(0.1, 0.5) \times (0 - h_{\min}, 0 + h_{\min})$ , thus the length are  $0.4\text{ m}$ ; see Figure 17a. The mechanical parameters are  $\nu = 0.2$  and  $E = 10^8\text{ Pa}$  and the fluid parameters are the same as in the previous example, where  $h_{\min} = 0.01\text{ m}$  and the time step is  $\delta t = 0.01\text{ s}$ . Here two injection stages are positioned at  $(0\text{ m}, 0.25\text{ m})$  and  $(0.25\text{ m}, 0\text{ m})$ , and we apply the suggested well model (33). The well model constants are chosen as  $r_e = 2^{0.25} \exp((-3\pi/4)h_{\min})$ ,  $r_w = 10^{-4}h_{\min}$ , for outer and inner radius, given initial well bore pressure is  $p_b = 50\text{ MPa}$ , and  $h_3 = 2\text{ m}$  for the depth of the well, following [16]. Figure 17 illustrates the fluid filled fracture propagation handling multiple injection points with the pressure values for each time step.

#### 4.6 Fracture Propagation in Layers with Different $G_c$ Values

In the last example, we study fracture propagation in a layered elastic media. Specifically,  $G_c$  is varied in the domain  $\Lambda = (0, 4\text{ m})^2$ . We focus on fracture propagation from a soft layer to a rigid layer as studied in [55]. The initial crack is centered at  $(2\text{ m}, 2.05\text{ m})$  with the length  $l = 0.225\text{ m}$ . Here  $h_{\min} = 0.011\text{ m}$  and the time steps are chosen as  $\delta t = 0.01\text{ s}$ . The fluid is injected at the center of the crack and the fluid, well model and the mechanical parameters are given as same as the previous well bore example. In this study, we separate the layers with different values for  $G_c$ . Here  $G_c = 10\text{ Pa m}$  for  $y > 3$ ,  $y < 1$ ,  $x > 3$  and  $x < 1$ . (the outer darker region in Figure 18), and  $G_c = 1$  for  $1 \leq y \leq 3$ , and  $1 \leq x \leq 3$ . We observe kinking of the fracture when it approaches the rigid layer and subsequent fracture growing along the layer in Figure 18.

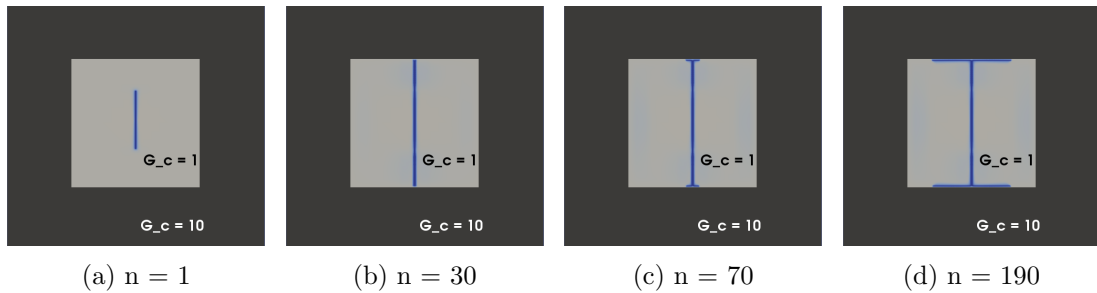


Figure 18: Example 4.6: Fracture propagating in surrounded layered media. The fracture is positioned at the soft layer and it propagates toward the rigid layer (darker region). We observe the kinked crack near the interface as we see from the experiment [55].

We finally observe that the active set solver performs well in all examples and shows similar convergence rates as presented in [24]. Moreover, the fixed-stress algorithm for phase field-based fracture coupled with the pressure diffusion problem works robustly but is not yet optimized with respect to stabilization parameters. Here, we refer to previous and related studies performed by [34] for the standard Biot system and recent extensions to a non-propagating lower-dimensional fracture in a porous medium [20]. Numerical analysis of further extensions to propagating fractures including phase field is nontrivial and currently underway.

## 5 Conclusion

In this paper, we presented a phase field formulation for pressurized and fluid filled crack propagation in porous media. The first novelty is a coupling of a pressure diffusion equation to a fully-coupled displacement-phase field approach. This coupling is realized in terms of a fixed-stress splitting in which we first solve for the pressure and then for the displacement-phase field variables. Here, the latter system is treated with a primal-dual active set approach that include treatment of the crack irreversibility. In addition to these algorithmic advancements, several numerical examples are consulted for verification in the case of pressurized fractures as well as demonstration of our scheme for fluid filled fractures in heterogeneous porous media. Specifically, we demonstrate that the phase field approach allows us to study complex fracture patterns including non-planar crack growth, joining and branching phenomena. In extension to existing studies, we also considered 3D simulations. From the computational point of view, local mesh adaptivity has been employed in order to enhance the local resolution of the phase field regularization parameter while keeping the computational cost reasonably low. Computational stability of our model has been shown for certain functionals on different spatial meshes. We believe that a decoupling approach, such as fixed-stress, will be useful for treating more complex flow in fractured porous media problems.

## Acknowledgments

The authors want to acknowledge that contributions from S. Lee were supported by funding from the Center for Frontiers of Subsurface Energy Security, an Energy Frontier Research Center funded by the U.S. Department of Energy, Office of Science, and Office of Basic Energy Sciences, DOE Project #DE-SC0001114. The research by M. F. Wheeler was partially supported by ConocoPhillips grant UTA 10-000444, Statoil grant STNO-4502931834, and T. Wick was partially supported by the Austrian

---

Academy of Sciences, The Institute for Computational Engineering and Sciences JT Oden fellowship, and the Center for Subsurface Modeling at UT Austin.

## References

- [1] G. Allaire, F. Jouve, and N. V. Goethem. Damage and fracture evolution in brittle materials by shape optimization methods. *Journal of Computational Physics*, 230(12):5010 – 5044, 2011. ISSN 0021-9991. doi: <http://dx.doi.org/10.1016/j.jcp.2011.03.024>.
- [2] M. Ambati, T. Gerasimov, and L. De Lorenzis. A review on phase-field models of brittle fracture and a new fast hybrid formulation. *Computational Mechanics*, 55(2):383–405, 2015.
- [3] L. Ambrosio and V. Tortorelli. Approximation of functionals depending on jumps by elliptic functionals via  $\gamma$ -convergence. *Comm. Pure Appl. Math.*, 43:999–1036, 1990.
- [4] L. Ambrosio and V. Tortorelli. On the approximation of free discontinuity problems. *Boll. Un. Mat. Ital. B*, 6:105–123, 1992.
- [5] H. Amor, J.-J. Marigo, and C. Maurini. Regularized formulation of the variational brittle fracture with unilateral contact: Numerical experiments. *Journal of Mechanics Physics of Solids*, 57:1209–1229, Aug. 2009. doi: 10.1016/j.jmps.2009.04.011.
- [6] M. Artina, M. Fornasier, S. Micheletti, and S. Perotto. Anisotropic mesh adaptation for crack detection in brittle materials. TUM Report, 2014.
- [7] W. Bangerth, T. Heister, G. Kanschat, and M. others. *Differential Equations Analysis Library*, 2012.
- [8] S. Berrone, S. Pieraccini, and S. Scial. An optimization approach for large scale simulations of discrete fracture network flows. *Journal of Computational Physics*, 256(0):838 – 853, 2014. ISSN 0021-9991. doi: <http://dx.doi.org/10.1016/j.jcp.2013.09.028>.
- [9] M. J. Borden, C. V. Verhoosel, M. A. Scott, T. J. R. Hughes, and C. M. Landis. A phase-field description of dynamic brittle fracture. *Comput. Meth. Appl. Mech. Engrg.*, 217:77–95, 2012.
- [10] B. Bourdin, G. Francfort, and J.-J. Marigo. Numerical experiments in revisited brittle fracture. *J. Mech. Phys. Solids*, 48(4):797–826, 2000.
- [11] B. Bourdin, G. Francfort, and J.-J. Marigo. The variational approach to fracture. *J. Elasticity*, 91(1–3):1–148, 2008.
- [12] B. Bourdin, C. Chukwudozie, and K. Yoshioka. A variational approach to the numerical simulation of hydraulic fracturing. SPE Journal, Conference Paper 159154-MS, 2012.
- [13] A. Bungler and A. Peirce. *Numerical Simulation of Simultaneous Growth of Multiple Interacting Hydraulic Fractures from Horizontal Wells*, chapter 21, pages 201–210. doi: 10.1061/9780784413654.021.
- [14] S. Burke, C. Ortner, and E. Süli. An adaptive finite element approximation of a generalized Ambrosio-Tortorelli functional. *M3AS*, 23(9):1663–1697, 2013.
- [15] S. Castonguay, M. Mear, R. Dean, and J. Schmidt. Predictions of the growth of multiple interacting hydraulic fractures in three dimensions. *SPE-166259-MS*, pages 1–12, 2013.

- 
- [16] Z. Chen and Y. Zhang. Well flow models for various numerical methods. *International Journal of Numerical Analysis and Modeling*, 6(3):375–388, 2009.
- [17] Z. Chen, A. Bungler, X. Zhang, and R. Jeffrey. Cohesive zone finite element based modeling of hydraulic fractures. *Acta Mechanica Solida Sinica*, 22:443–452, 2009.
- [18] G. Francfort and J.-J. Marigo. Revisiting brittle fracture as an energy minimization problem. *J. Mech. Phys. Solids*, 46(8):1319–1342, 1998.
- [19] B. Ganis, M. Mear, A. Sakhaee-Pour, M. Wheeler, and T. Wick. Modeling fluid injection in fractures with a reservoir simulator coupled to a boundary element method. *Computational Geosciences*, 18(5):613–624, 2014. ISSN 1420-0597. doi: 10.1007/s10596-013-9396-5.
- [20] V. Girault, K. Kumar, and M. Wheeler. Convergence of iterative coupling of geomechanics with flow in a fractured poroelastic medium. ICES report 15-05, Feb 2015.
- [21] E. Gordeliy and A. Peirce. Coupling schemes for modeling hydraulic fracture propagation using the xfem. *Comp. Meth. Appl. Mech. Engrg.*, 253:305–322, 2013.
- [22] E. Gordeliy and A. Peirce. Implicit level set schemes for modeling hydraulic fractures using the xfem. *Comp. Meth. Appl. Mech. Engrg.*, 266:125–143, 2013.
- [23] P. Gupta and C. A. Duarte. Simulation of non-planar three-dimensional hydraulic fracture propagation. *International Journal for Numerical and Analytical Methods in Geomechanics*, 38(13):1397–1430, 2014. ISSN 1096-9853. doi: 10.1002/nag.2305.
- [24] T. Heister, M. F. Wheeler, and T. Wick. A primal-dual active set method and predictor-corrector mesh adaptivity for computing fracture propagation using a phase-field approach. *Comput. Methods Appl. Mech. Engrg.*, 290:466–495, 2015.
- [25] M. Heroux, R. Bartlett, V. H. R. Hoekstra, J. Hu, T. Kolda, R. Lehoucq, K. Long, R. Pawlowski, E. Phipps, A. Salinger, H. Thornquist, R. Tuminaro, J. Willenbring, and A. Williams. An Overview of Trilinos. Technical Report SAND2003-2927, Sandia National Laboratories, 2003.
- [26] M. Hintermüller, K. Ito, and K. Kunisch. The primal-dual active set strategy as a semismooth newton method. *SIAM Journal on Optimization*, 13(3):865–888, 2002.
- [27] A. Katiyar, J. T. Foster, H. Ouchi, and M. M. Sharma. A peridynamic formulation of pressure driven convective fluid transport in porous media. *Journal of Computational Physics*, 261(0):209 – 229, 2014. ISSN 0021-9991. doi: <http://dx.doi.org/10.1016/j.jcp.2013.12.039>.
- [28] O. Kresse, X. Weng, H. Gu, and R. Wu. Numerical modeling of hydraulic fracture interaction in complex naturally fractured formations. *Rock Mech. Rock Eng.*, 46(3):555–558, 2013.
- [29] B. Lecampion. An extended finite element method for hydraulic fractures. *Communications in Numerical Methods in Engineering*, 25(2):121–133, 2009.
- [30] B. Meyer and L. Bazan. A discrete fracture network model for hydraulically induced fractures-theory, parametric and case studies. In Proceedings SPE Hydraulic Fracturing Technology Conference and Exhibition. The Woodlands, Texas, USA. SPE 140514, 2011.
- [31] C. Miehe, M. Hofacker, and F. Welschinger. A phase field model for rate-independent crack propagation: Robust algorithmic implementation based on operator splits. *Comput. Meth. Appl. Mech. Engrg.*, 199:2765–2778, 2010.

- 
- [32] C. Miehe, F. Welschinger, and M. Hofacker. Thermodynamically consistent phase-field models of fracture: variational principles and multi-field fe implementations. *International Journal of Numerical Methods in Engineering*, 83:1273–1311, 2010.
- [33] C. Miehe, S. Mauthe, and S. Teichtmeister. Minimization principles for the coupled problem of darcybiot-type fluid transport in porous media linked to phase field modeling of fracture. *Journal of the Mechanics and Physics of Solids*, 82:186 – 217, 2015. ISSN 0022-5096. doi: <http://dx.doi.org/10.1016/j.jmps.2015.04.006>. URL <http://www.sciencedirect.com/science/article/pii/S0022509615000733>.
- [34] A. Mikelić and M. F. Wheeler. Convergence of iterative coupling for coupled flow and geomechanics. *Comput Geosci*, 17(3):455–462, 2012.
- [35] A. Mikelić, B. Wang, and M. Wheeler. Numerical convergence study of iterative coupling for coupled flow and geomechanics. *Computational Geosciences*, 18(3-4):325–341, 2014. ISSN 1420-0597. doi: 10.1007/s10596-013-9393-8.
- [36] A. Mikelić, M. Wheeler, and T. Wick. Phase-field modeling of a fluid-driven fracture in a poroelastic medium. *Computational Geosciences*, pages 1–25, 2015. ISSN 1420-0597. doi: 10.1007/s10596-015-9532-5. URL <http://dx.doi.org/10.1007/s10596-015-9532-5>.
- [37] A. Mikelić, M. F. Wheeler, and T. Wick. A phase-field method for propagating fluid-filled fractures coupled to a surrounding porous medium. *SIAM Multiscale Model. Simul.*, 13(1):367–398, 2015.
- [38] A. Mikelić, M. F. Wheeler, and T. Wick. A quasi-static phase-field approach to pressurized fractures. *Nonlinearity*, 28(5):1371–1399, 2015.
- [39] B. Noetinger. A quasi steady state method for solving transient darcy flow in complex 3d fractured networks accounting for matrix to fracture flow. *Journal of Computational Physics*, 283(0):205 – 223, 2015. ISSN 0021-9991. doi: <http://dx.doi.org/10.1016/j.jcp.2014.11.038>.
- [40] J. Olson. Multi-fracture propagation modeling: Applications to hydraulic fracturing in shales and tight gas sands. In *Proceedings 42nd U.S. Rock Mechanics Symposium. San Francisco, CA, USA. Paper No. 08-327*, 2008.
- [41] J. Olson et al. Multi-fracture propagation modeling: Applications to hydraulic fracturing in shales and tight gas sands. In *The 42nd US rock mechanics symposium (USRMS)*. American Rock Mechanics Association, 2008.
- [42] D. Peaceman. Interpretation of well-block pressures in numerical reservoir simulation. *Society of Petroleum Engineers*, 1978. doi: 10.2118/6893-PA,SPE-6893-PA.
- [43] D. Peaceman. Interpretation of well-block pressures in numerical reservoir simulation with non-square grid blocks and anisotropic permeability. *Society of Petroleum Engineers*, 1983. doi: 10.2118/10528-PA,SPE-10528-PA.
- [44] A. Peirce and E. Detournay. An implicit level set method for modeling hydraulically driven fractures. *Comput. Meth. Appl. Mech. Engrg.*, 197:2858–2885, 2008.
- [45] E. Remij, J. Remmers, J. Huyghe, and D. Smeulders. The enhanced local pressure model for the accurate analysis of fluid pressure driven fracture in porous materials. *Computer Methods in Applied Mechanics and Engineering*, 286(0):293 – 312, 2015. ISSN 0045-7825. doi: <http://dx.doi.org/10.1016/j.cma.2014.12.025>.

- 
- [46] Q. Ren, Y. Dong, and T. Yu. Numerical modeling of concrete hydraulic with extended finite element method. *Science in China Series E: Technological Science*, 52(3):559–565, 2009.
- [47] T. Sandve, I. Berre, and J. Nordbotten. An efficient multi-point flux approximation method for discrete fracturematrix simulations. *Journal of Computational Physics*, 231(9):3784 – 3800, 2012. ISSN 0021-9991. doi: <http://dx.doi.org/10.1016/j.jcp.2012.01.023>.
- [48] A. Schlüter, A. Willenbücher, C. Kuhn, and R. Müller. Phase field approximation of dynamic brittle fracture. *Comput. Mech.*, 54:1141–1161, 2014.
- [49] I. N. Sneddon and M. Lowengrub. *Crack problems in the classical theory of elasticity*. SIAM series in Applied Mathematics. John Wiley and Sons, Philadelphia, 1969.
- [50] A. Taleghani. *Analysis of hydraulic fracture propagation in fractured reservoirs: an improved model for the interaction between induced and natural fractures*. PhD thesis, The University of Texas at Austin, 2009.
- [51] C. V. Verhoosel and R. de Borst. A phase-field model for cohesive fracture. *International Journal for Numerical Methods in Engineering*, 96(1):43–62, 2013. ISSN 1097-0207. doi: 10.1002/nme.4553. URL <http://dx.doi.org/10.1002/nme.4553>.
- [52] M. Wheeler, T. Wick, and W. Wollner. An augmented-Lagangrian method for the phase-field approach for pressurized fractures. *Comp. Meth. Appl. Mech. Engrg.*, 271:69–85, 2014.
- [53] T. Wick, S. Lee, and M. Wheeler. 3D phase-field for pressurized fracture propagation in heterogeneous media. *VI International Conference on Computational Methods for Coupled Problems in Science and Engineering 2015 Proceedings*, May 2015.
- [54] T. Wick, G. Singh, and M. Wheeler. Fluid-filled fracture propagation using a phase-field approach and coupling to a reservoir simulator. *SPE Journal*, pages 1–19, 2015. doi: 10.2118/168597-PA.
- [55] H. Wu, A. Chudnovsky, and J. D. abd G.K. Wong. A map of fracture behavior in the vicinity of an interface, 2004.
- [56] X. Zhang, R. Jeffrey, and M. Thiercelin. Deflection and propagation of fluid-driven fractures at frictional bedding interfaces: A numerical investigation. *J. Struct. Geol.*, 29(3):396–410, 2007.